Elsevier Editorial System(tm) for Building and Environment
Manuscript Draft

Manuscript Number: BAE-D-15-00449R3

Title: City breathability in medium density urban-like geometries evaluated through the pollutant transport rate and the net escape velocity

Article Type: Original Research Paper

Keywords: Urban canopy layer; pollutant transport rate; contribution ratio; net escape velocity; computational fluid dynamics

Corresponding Author: Dr. Riccardo Buccolieri, Ph.D.

Corresponding Author's Institution: University of Salento

First Author: Jian Hang, PhD

Order of Authors: Jian Hang, PhD; Qun Wang, Mphil; Xieyuan Chen, Mphil; Mats Sandberg, PhD, Prof; Wei Zhu, Mphil; Riccardo Buccolieri, PhD; Silvana Di Sabatino, PhD, Prof

Abstract: This paper investigates pollutant removal at pedestrian level in urban canopy layer (UCL) models of medium packing density (lambda_p=lambda_f=0.25) using computational fluid dynamics (CFD) simulations. The effects of urban size, building height variations, wind direction and uniform wall heating are investigated. The standard and RNG k-epsilon turbulence models, validated against wind tunnel data, are used. The contribution of mean flows and turbulent diffusion in removing pollutants at pedestrian level is quantified by three indicators: the net escape velocity (NEV), the pollutant transport rate (PTR) across UCL boundaries and their ratios (CR).
Results show that under parallel approaching wind, after a wind-adjustment region, a fully-developed region develops. Longer urban models attain smaller NEV due to pollutant accumulation. Specifically, for street-scale models (~100m), most pollutants are removed out across leeward street openings and the dilution by horizontal mean flows contributes mostly to NEV. For neighbourhood-scale models (~1km), both horizontal mean flows and turbulent diffusion contribute more to NEV than vertical mean flows which instead produce significant pollutant re-entry across street roofs. In contrast to uniform height, building height variations lead to an increase of the contribution of vertical mean flows, but only slightly influence NEV. Finally, flow conditions with parallel wind and wall heating attain larger NEV than oblique wind and isothermal condition.
The paper proves that by analysing the values of the three indicators it is possible to form maps of urban breathability according to prevailing wind conditions and known urban morphology that can be of easy use for planning purposes.

City breathability in medium density urban-like geometries evaluated through the pollutant transport rate and the net escape velocity

Jian Hang[a], Qun Wang[a], Xieyuan Chen[a], Mats Sandberg[b], Wei Zhu[a], Riccardo Buccolieri[c*], Silvana Di Sabatino[d]

[a]Department of Atmospheric Sciences, School of Environmental Science and Engineering of Sun Yat-Sen University, Guangzhou, P. R. China

[b]Laboratory of Ventilation and Air Quality, University of Gävle, SE-80176 Gävle, Sweden

[c]Dipartimento di Scienze e Tecnologie Biologiche ed Ambientali, University of Salento, S.P. 6 Lecce-Monteroni, 73100 Lecce, Italy

[d]Department of Physics and Astronomy, ALMA MATER STUDIORUM - University of Bologna, Viale Berti Pichat 6/2, 40127 Bologna

*Corresponding author. Tel.: +39 0832 297 115; fax: +39 0832 297 112.

E-mail address: riccardo.buccolieri@unisalento.it (R. Buccolieri).

Abstract

This paper investigates pollutant removal at pedestrian level in urban canopy layer (UCL) models of medium packing density (λ_p=λ_f=0.25) using computational fluid dynamics (CFD) simulations. The effects of urban size, building height variations, wind direction and uniform wall heating are investigated. The standard and RNG k-ε turbulence models, validated against wind tunnel data, are used. The contribution of mean flows and turbulent diffusion in removing pollutants at pedestrian level is quantified by three indicators: the net escape velocity (*NEV*), the pollutant transport rate (*PTR*) across UCL boundaries and their ratios (*CR*).

Results show that under parallel approaching wind, after a wind-adjustment region, a fully-developed region develops. Longer urban models attain smaller *NEV* due to pollutant accumulation. Specifically, for street-scale models (~100m), most pollutants are removed out across leeward street openings and the dilution by horizontal mean flows contributes mostly to *NEV*. For neighbourhood-scale models (~1km), both horizontal mean flows and turbulent diffusion contribute more to *NEV* than vertical mean flows which instead produce significant pollutant re-entry across street roofs. In contrast to uniform height, building height variations

lead to an increase of the contribution of vertical mean flows, but only slightly influence *NEV*. Finally, flow conditions with parallel wind and wall heating attain larger *NEV* than oblique wind and isothermal condition.

The paper proves that by analysing the values of the three indicators it is possible to form maps of urban breathability according to prevailing wind conditions and known urban morphology that can be of easy use for planning purposes.

Keywords**:** Urban canopy layer; pollutant transport rate; contribution ratio; net escape velocity; computational fluid dynamics.

1. Introduction

The increase of vehicle emissions in cities and the ongoing urbanization worldwide continue to deteriorate urban air quality within the urban canopy layer (UCL) [1-2] which produces adverse effect to the health of people indoor and outdoor [3-4]. Besides reducing pollutant emissions, improving urban ventilation through use of architectural modifications may help street-level pollutant dilution [5-14].

Flow and pollutant dispersion within and above urban areas are commonly classified into four length scales, i.e. street-scale (~100m), neighbourhood-scale (~1km), city-scale (~10km) and meso-scale (~1000km) [15-18]. The former three scales are micro-scale (~100m-10km) for which the flow below building rooftops are explicitly solved. At this scale, due to pollutant accumulation effect, urban air quality depends upon their neighbourhoods and city-scale characteristics [15-16]. Meso-scale modelling is usually employed to investigate regional pollutant transport in which urban areas are treated as roughness elements thus providing boundary conditions for smaller scale studies [17]. Within this framework flow and pollutant dispersion from street-scale to neighbourhood-scale have been widely investigated often coupling wind tunnel/field experiments with computational fluid dynamics (CFD) simulations [5-14, 19-23, 25-39, 43-45]. CFD modelling has been rarely applied to city-scale (~10km) because it still requires too high computational costs to simulate urban airflows through thousands of buildings [18].

Street-scale and neighbourhood-scale studies usually disregard the larger-scale boundaries and emphasize the local parameters. For two-dimensional (2D) street canyon models, four flow regimes dependent on street aspect ratios (building height/street width, H/W) are reported [19-

23], i.e. the isolated roughness flow regime (H/W<0.3), the wake interference flow regime (0.3<H/W<0.67), the skimming flow regime with one main vortex (0.67<H/W<1.67), and multi-vortex flow regime (H/W>1.67). For three-dimensional (3D) urban models, major urban morphological parameters are the building planar area index λ_p (i.e. the ratio between the planar area of buildings viewed from above and the total floor area) and the frontal area index λ_f (i.e. the ratio of the frontal area of buildings to the total floor area) [24]. 3D spare urban areas (for example λ_f=0.0625) are more effective in removing pollutant [13], but have a lower efficiency of land utilization. Densely built-up urban areas usually results in poor ventilation conditions [7, 9-14]. The most typical parameters of real urban areas are λ_p=λ_f=0.25 [24]. As building packing densities are fixed, some other urban parameters are significant, including urban forms [8, 10-11], urban size and building height variations [7-8, 12, 29], ambient wind directions [5, 8, 14, 26-29] etc. Thermal effect is another key factor. Field measurements showed temperature difference between air and building surfaces can reach up to 12-14°C [31-32]. If Richardson number (Froude number) is relatively large (small), the buoyancy force induced by air-wall temperature difference can affect or even dominate urban airflows [31-40]. On the other hand, Giovannini et al. [46] showed using temperature data recorded in urban street canyons that when solar radiation is weak or absent, the temperature field remains mostly homogeneous.

In this context, fixing the medium building packing density (λ_f=λ_p=0.25), we aim to quantify how urban sizes, building height variations, ambient wind directions and wall heating affect the capacity of removing pollutants at pedestrian level. To this purpose, pollutant transport rate (*PTR*) and its ratio (i.e. contribution ratio) (*CR*) [7] are applied to evaluate the relative contribution in pollutant removal by mean flows and turbulent diffusion across UCL boundaries. A new concept, the net escape velocity [41], is used to quantify the net capacity of pollutant dilution at pedestrian level.

2. CFD methodology and case studies

Ansys FLUENT was used to solve the steady-state flow field [42] by employing the RNG and the standard k-ε model. We are aware that deficiencies of the steady RANS approach with the standard k-ε model include the stagnation point anomaly with overestimation of turbulence kinetic energy near the frontal corner and the resulting underestimation of the size of separation and recirculation regions on the roof and the side faces, as well as the underestimation of

turbulence kinetic energy in the wake resulting in an overestimation of the size of the cavity zone and wake. These limitations can be explicitly resolved by Large Eddy Simulation (LES). There are however still challenges facing LES such as the development of advanced sub-grid scale models, the strongly increased computational requirements and the difficulty in specifying appropriate time-dependent inlet and wall boundary conditions. Therefore, in quantitative work one is obliged to use turbulence models based on using Averaged Navier-Stokes (NS) equations and, in addition, a set of equations that express the relations between terms appearing in the averaged equations. Actually, in spite of its deficiencies, steady RANS modelling with the k–ε model or with other turbulence models has become the most popular CFD approaches for pedestrian-level wind studies. There are quite some indications from recent studies supported by extensive solution verification and validation actions that steady RANS has a fairly high accuracy in predicting the mean wind speed at least for regions with high amplification factor [26, 43, 47-48].

2.1 Flow set-up in the CFD validation case

Wind tunnel data was first used to evaluate the reliability of CFD simulations. In wind tunnel experiments (see Fig. 1a), a 7-row and 13-column cube building array with a parallel approaching wind was investigated [44]. Building width (B), building height (H) and street width (W) were equal to 15cm (λ_p=λ_f=0.25, H/W=1) at a scale ratio of 1:200. As shown in Fig. 1a, x, y and z are the stream-wise, span-wise (lateral) and vertical directions. x/H=0 represents the location of windward street opening. Point Vi represents the centre point of the secondary street No i. Vertical profiles of stream-wise velocity $\overline{u}(z)$, vertical velocity $\overline{w}(z)$ and turbulence kinetic energy $k(z)$ at Points Vi were measured.

The same 7-row cube array was reproduced in the CFD validation case. Since the wind-tunnel building array was sufficiently wide in the lateral (y) direction, turbulent airflow in the middle main column was mainly affected by the external flow above it. To reduce the computational load, only half of this column was considered (see Fig. 1a) [44-45]. Fig. 1b-1c show model geometry, CFD domain and boundary conditions in this validation case. In particular, the distances of UCL boundary to domain top, outlet and inlet were set 9.0H, 40.3H and 6.7H, respectively (Fig. 1c). Zero normal gradient was used at the domain top, domain outlet, and two lateral domain boundaries.

At domain inlet, the vertical profile of stream-wise velocity measured in the upstream free flow together with $k(z)$ and its dissipation rate (ε) (see Eq. (1)) were used to provide boundary conditions [44-45]. It represented a neutral atmospheric boundary layer with a full-scale surface roughness z_0=0.1m and flowing above open rural area with a regular cover of low crop [45].

$$U_0(z) = U_H(z/H)^{0.16} \tag{1a}$$

$$k(z) = u_*^2 / \sqrt{C_\mu} \tag{1b}$$

$$\varepsilon(z) = C_\mu^{3/4} k^{3/2} / (\kappa_v z) \tag{1c}$$

where C_μ is 0.09, u_*=0.24ms^{-1} is the friction velocity, κ_v =0.4 is von Karman's constant, U_H=3.0ms^{-1} is the undisturbed reference velocity at z=H.

No slip boundary condition with standard wall function [42] was used at all wall surfaces. To reproduce a horizontally homogeneous atmospheric boundary layer (ABL) surrounding urban areas, we followed best practice guidelines for setting the upstream and downstream ground [49-51]. Using a standard wall function [42], the roughness height k_S and the roughness constant C_S are determined from their appropriate relationship with z_0 as follows [49]:

$$ks = \frac{9.793 z_0}{C_S} \tag{2}$$

Note that Fluent 6.3 does not allow k_S to be larger than the distance between the centre point P of the wall adjacent cell and the wall (y_P) [49]. If the user implements a larger value, the code will automatically set k_S equal to y_P without warning. Therefore according to van Hooff and Blocken [50-51], a user-defined function was used to set the roughness constant C_S=4 because the Fluent 6.3 code does not allow it to be larger than 1. To summarize, for the ground surface we used k_S=0.245m and C_S=4 for z_0=0.1 m to ensure the roughness height k_S wass below y_P=0.25m.

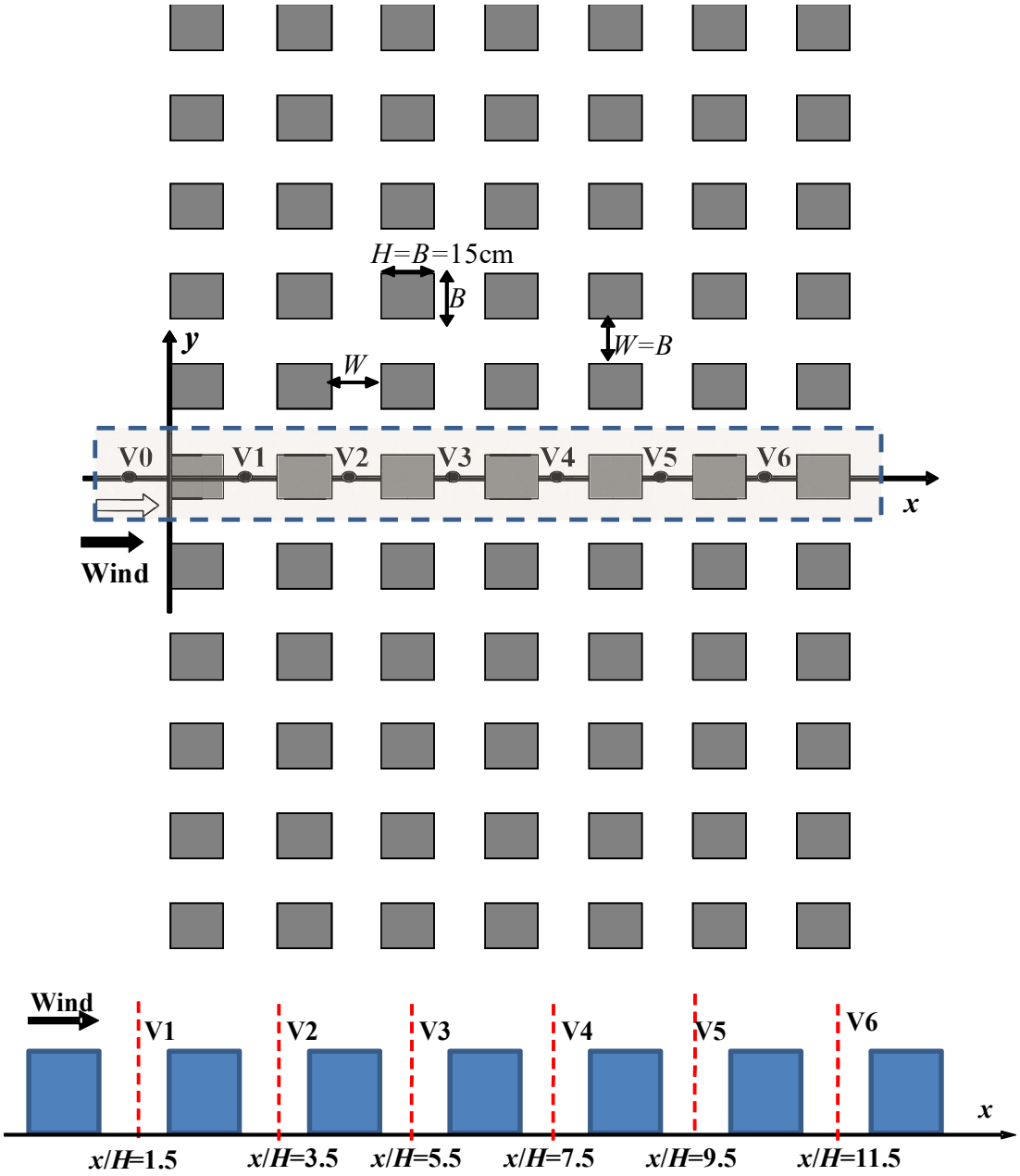

(a)

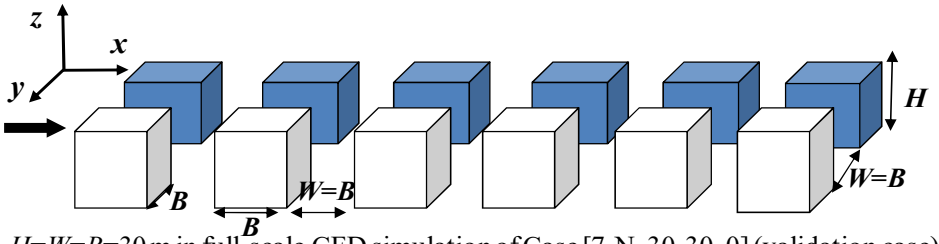

H=*W*=*B*=30 m in full-scale CFD simulation of Case [7-N, 30-30, 0] (validation case)

(b)

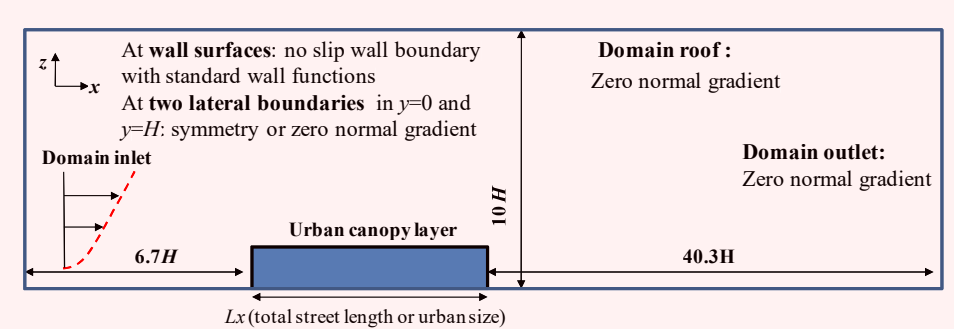

(c)

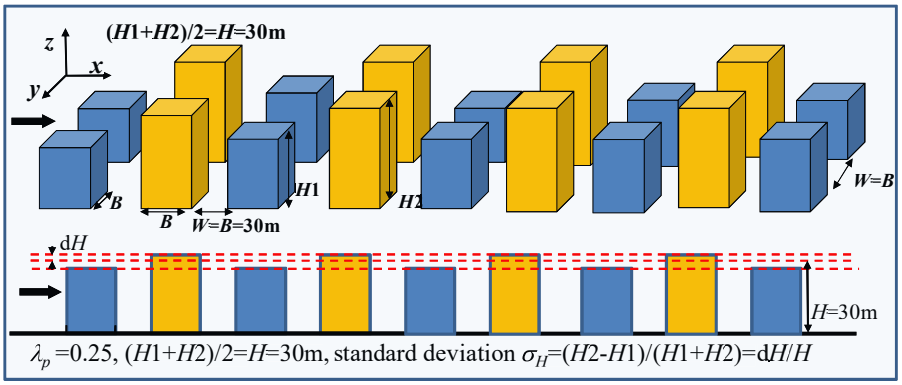

(d)

Fig. 1. (a) Array used in the wind tunnel experiments, (b) model in the CFD validation case, (c) computational domain in Group I (see Table 1), (d) model with regular building height variations.

For this CFD validation case, a grid convergence study was performed using a coarse grid (303,408 hexahedral cells), a medium grid (531,657 hexahedral cells) and fine grid (1,024,992 hexahedral cells). The minimum cell size near the ground and building wall surfaces were 0.75m for the coarse grid, 0.5m for the medium grid and 0.3m for the fine grid. The grid independence study (see subsection 3.1) showed the medium grid was appropriate since it predicted turbulent flow field similarly well as the fine grid. With this medium grid arrangement, the cell size nearest to the street ground was 0.5m (H/60) and four hexahedral cells were used below the pedestrian level (z=0m to 2m). Moreover, the cell size near all wall surfaces ranged from 0.5m (H/60) to 1m (H/30) and the grid expansion ratio from wall surfaces to the surrounding was smaller than 1.15.

2.2 Model description and flow set-up in all test cases (cfr. Table 1)

As shown in Table 1, all test cases in CFD simulations are classified into two groups

(Group I and II). Each case is named as Case [number of rows-number of columns, H_1-H_2, wind direction]. The number of rows and columns refer to as the numbers of the main and secondary streets. H_1 and H_2 denote building heights for rows of an odd and even number. Wind directions (0^o, 15^o, 30^o, 45^o) are the angles between the approaching wind and the main streets. For example, the CFD validation case (subsection 2.1) is named as Case [7-N, 30-30, 0], representing a 7-row cube array with a parallel approaching wind (0^o). The column number "N" denotes the span-wise urban size (Ly) is sufficiently large to neglect the effect of lateral UCL boundaries.

For all test cases in Group I (Table 1, see Fig. 1b-1d), UCL lateral boundaries were disregarded with a parallel approaching wind (0^o). The effects of stream-wise urban size (Lx), building height variations and uniform wall heating were investigated. For test cases with a uniform height (Case [i-N,30-30,0], see Fig. 1b), Lx increases from street-scale (i=7, Lx=390m) to neighbourhood-scale (i=70, Lx=4170m) with only isothermal conditions. For test cases with building height variations (Case [14-N, H1-H2,0] and Case [28-N, H1-H2,0]), the standard deviation of building heights $\sigma_H = (H2-H1)/(H2+H1)$ ranges from 0% to 83.3% with the same average height H_0=30m (see Fig. 1d), with isothermal conditions and uniform wall heating. CFD domain size and boundary conditions were similar as the CFD validation case. Only half of the middle column was considered to reduce the grid number and calculation time for neighbourhood-scale flow modelling. The distances from UCL boundaries to domain roof, domain outlet and domain inlet are 9.0H, 40.3H, 6.7H, respectively. Zero normal gradient was used at the domain top, domain outlet, and two lateral domain boundaries.

For Group II (Table 1), the effects of lateral UCL boundaries and wind directions were investigated. Fig. 2 shows CFD domain, boundary conditions and grid arrangements in two example cases. With the parallel wind (Case [m-n,30-30,0], with m=n=5,7,9,11, θ=0^o), only half domain was used (see Fig. 2a). The distance of UCL boundaries to domain roof, outlet, inlet and lateral boundaries were set 9H, 40.3H, 6.7H, 10H. Zero-normal gradient condition was used at domain outlet, domain roof, and the lateral domain boundaries. At domain inlet, vertical profiles of Eq. (1) were used. For test cases Case [5-5, 30-30, θ] and Case [7-7, 30-30, θ] with oblique winds (θ=15^o, 30^o , 45^o, Fig. 2b-2c), full CFD domain was used with two domain inlets and two domain outlets. The distances of UCL boundaries to domain roof, outlets and inlets were 9H, 41H and 6.7H. At domain outlets and domain roof, zero normal gradient condition was used. At domain inlets, vertical profiles of $\bar{u}(z) = U_0(z)\cos\theta$ in x direction, $\bar{v}(z) = U_0(z)\sin\theta$ in y direction,

vertical velocity $\overline{w}(z)=0$ and turbulent quantities (see Eq. (1b)-(1c)) were used.

As for the validation case, for all test cases in Table 1, the medium grid arrangement was adopted. The total number of hexahedral cells ranged from half million to 4.7 million.

Table 1. Summary of UCL models investigated (λ_p=λ_f=0.25).

Case name (Group I)	Number of rows /stream-wise urban size (*Lx*)	Span-wise urban size (*Ly*)	Source $\dot{M}/\dot{M}_0$	Building heights (*H*1-*H*2) and σ_H	Wind direction / heating condition
[7-N,30-30,0] (validation case)	7 rows, *Lx*=390m	Column no N or *Ly* is large enough to neglect lateral boundary effect	1.00	30m-30m, σ_H=0%	0^o (parallel wind) Isothermal condition
[14-N,30-30,0]	14 rows, *Lx*=810m		2.00		
[21-N,30-30,0]	21 rows, *Lx*=1230m		3.05		
[28-N,30-30,0]	28 rows, *Lx*=1650m		4.10		
[35-N,30-30,0]	35 rows, *Lx*=2070m		5.15		
[42-N,30-30,0]	42 rows, *Lx*=2490m		6.21		
[49-N,30-30,0]	49 rows, *Lx*=2910m		7.26		
[56-N,30-30,0]	56 rows, *Lx*=3330m		8.31		
[63-N,30-30,0]	63 rows, *Lx*=3750m		9.36		
[70-N,30-30,0]	70 rows, *Lx*=4170m		10.41		
[14-N,30-30,0]	*Lx*=810m		2.0	30m-30m σ_H=0%	
[14-N,25-35,0]				25m-35m, 16.7%	
[14-N,20-40,0]				20m-40m, 33.3%	
[14-N,15-45,0]				15m-45m, 50.0%	
[14-N,10-50,0]				10m-50m, 66.7%	
[14-N,5-55,0]				5m-55m, 83.3%	
[28-N,30-30,0]	*Lx*=1650m		4.1	σ_H=0%	0^o **Isothermal or all wall heating (100 W/m^2)**
[28-N,25-35,0]				σ_H=16.7%	
[28-N,20-40,0]				σ_H=33.3%	
[28-N,15-45,0]				σ_H=50.0%	
[28-N,10-50,0]				σ_H=66.7%	
[28-N,5-55,0]				σ_H=83.3%	
Case name (Group II)	Number of rows/ *Lx*	*Ly*	Source $\dot{M}/\dot{M}_0$	Building heights (*H*1-*H*2) and σ_H	Wind direction/ heating condition

[5-5,30-30,0]	5 rows, *Lx*=270m	*Ly*=270m	5.62	30m-30m σ_H=0%	0 ° Isothermal
[7-7,30-30,0]	7 rows, *Lx*=390m	*Ly*=390m	12.16		
[9-9,30-30,0]	9 rows, *Lx*=510m	*Ly*=510m	20.88		
[11-11,30-30,0]	11 rows, *Lx*=630m	*Ly*=630m	31.63		
[5-5,30-30,0]	*Lx*=270m	*Ly*=270m	5.62	30m-30m σ_H=0%	0 °,15 °,30 °,45 ° Isothermal
[5-5,30-30,15]					
[5-5,30-30,30]					
[5-5,30-30,45]					
[7-7,30-30,0]	*Lx*=390m	*Ly*=390m	12.16	30m-30m σ_H=0%	
[7-7,30-30,15]					
[7-7,30-30,30]					
[7-7,30-30,45]					

* The deviation of height variation is $\sigma_H=(H2-H1)/(H2+H1)$. $\dot{M}/\dot{M}_0$ is the normalized total pollutant release rate.

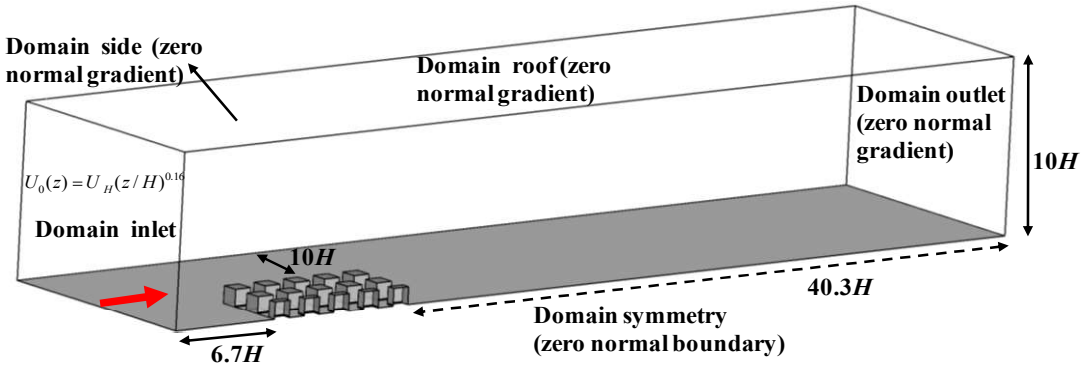

(a)

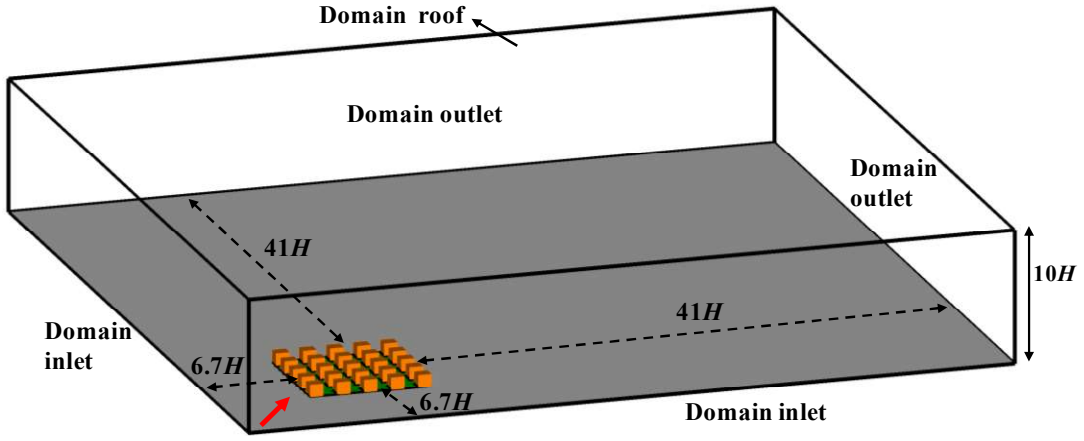

(b)

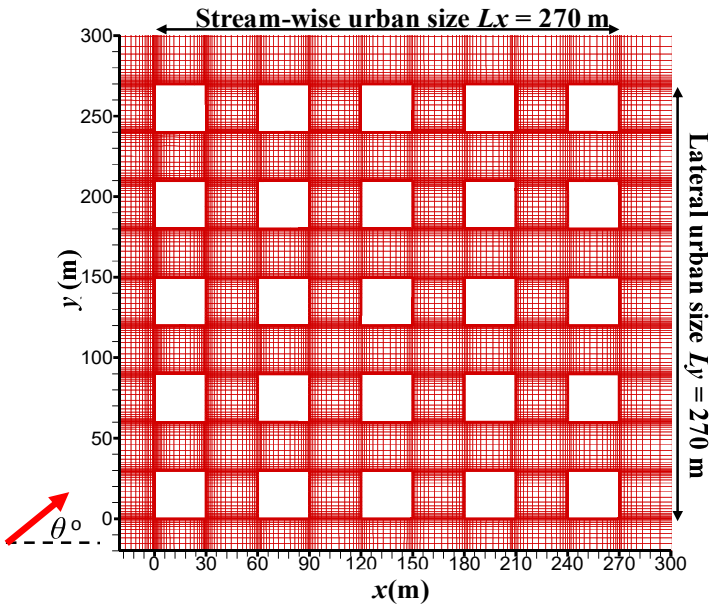

(c)

Fig. 2. Computational domain in Group II (see Table 1): (a) 0° (half domain) and (b) oblique wind (full domain), (c) Grid in *x*-*y* plane in Case [5-5, 30-30, θ].

Uniform wall heating set-up at all wall surfaces:

For test cases Case [14-N, H1-H2, 0] and Case [28-N, H1-H2, 0] (Table 1, Group I), uniform sensible heat flux Q_b at all building façades and street ground was also considered. The choice of Q_b=100 W/m^2 was based on the specific literature [9, 53] being the maximum daily sensible heat flux with the order of 100W/m^2 (usually it is not much greater than 300W/m^2 in most places, see [53]) Field measurements of urban surface temperature profiles in Hong Kong also confirmed that the calculated sensible heat flux can reach this value [31]. The ambient temperature at domain inlet was set to 20°C. Zero normal heat flux condition (adiabatic) was defined at the domain bottom outside of urban area. The Boussinesq model was employed for the buoyancy effect.

It is worth noting that there are different realistic situations of surface heat fluxes in the 2D street canyon [32-34, 36-40] or 3D urban areas [31, 35, 55]. The present case of uniform sensible heat flux at all wall surfaces is more a modelling exercise rather than a study of all the realistic situations. However, it may represent a realistic distribution of street canyon surfaces at night after sunset when urban heat island intensity is nearly at its maximum and it is expected that the sensible heat flux from building surfaces is large and buoyancy effect on airflow is maximum. It

is also worth to mentioning that, at night, radiation heat loss from buildings to the sky might be similar to or larger than natural convection depending on the sky/cloud conditions. Besides there are some other terms in the urban energy balance, such as latent heat loss, anthropogenic heat flux etc. Similar to the literature [33-34, 36-40, 55], to simplify the physical model, uniform constant wall temperature or uniform heat fluxes from wall surfaces were usually used in wind tunnel measurement or CFD simulations. For example, by using wind tunnel experiments and CFD simulations by RANS turbulence models, Allegrini et al. [36-37] confirmed that uniform heating at leeward wall, ground and all wall surfaces can enhance recirculation airflows except windward wall heating. By employing RANS turbulence models, Santiago et al. [55] analysed realistic effects of urban surface heat fluxes (for different solar position) on airflow in periodic urban unit with the same building packing densities. Overall, these investigations confirmed that all wall heating (similar to our case) can significantly enhance urban airflows when the Richardson number (Froude number) is relatively large (small). This paper mainly emphasizes the effect of sensible heat flux from all building surfaces by convection.

In addition, among RANS turbulence models, low-Reynolds models with enhanced wall treatment were found to work better than high-Reynolds ones in predicting convective heat transfer with air-wall temperature difference. However, it typically requires a dimensionless wall distance ($y+$) of about 1 to resolve the viscous sub-layer near wall surfaces. The required high computational resources precluded the possibility of adopting this approach in simulating 3D urban airflow with groups of buildings. However, previous studies indicated the RNG and standard k-ε models with standard wall function can be employed to investigate the wall flow with uniform wall heat fluxes by neglecting the detailed heat transfer process near wall surfaces [54-55]. Thus, this paper adopted a similar technique to study the effect of uniform wall heating on urban airflow and ventilation at pedestrian level.

Overall, CFD set-up fulfils the major requirements provided by CFD guidelines [52]. All transport equations were discretized by the second-order upwind scheme. The SIMPLE scheme was used for the pressure and velocity coupling. The under-relaxation factors for pressure term, momentum, k and ε are 0.3, 0.7, 0.5 and 0.5 respectively. CFD simulations were first run for about 4,000 iterations with first-order upwind scheme, and then continued with the second-order upwind scheme until all residuals became constant. The residuals reached the following minimum values or less: 10^{-4} for the continuity equation, 0.5×10^{-5} for the velocity components

and k, 0.5×10^{-5} and 0.5×10^{-4} for pollutant concentration and ε. Each case was computed in a 2-node CPU cluster, and each node had sixteen processors (2.4 GHz Intel 64). The calculation time of each case was about 4 hours to 2 days depending on the total grid number and turbulence models used (RNG k-ε requires shorter time). After attaining the steady-state solutions for the airflow field, tracer gas was continuously released at the pedestrian level for investigating pollutant dispersion and ventilation assessment.

2.3 Dispersion set-up and ventilation indicators

As reviewed by Chen [59], tracer gas technique with the uniform tracer gas (pollutant) source has been widely applied for indoor ventilation analysis. Those ventilation concepts may be retrieved from tracer gas concentrations in the final steady state [41, 56-59]. Recently, some researchers have applied such tracer gas technique and indoor ventilation concepts for outdoor ventilation assessment [5, 7-9, 12-14] in which uniform tracer gas (pollutant) sources in an urban domain, in the entire pedestrian level or in the entire urban canopy layers were defined. Among the ventilation indicators we remind here the purging flow rate and the pollutant transport rate [5, 7], the age of air and the air exchange efficiency [8-9, 12], the city breathability [13-14] etc. have been applied to quantify urban ventilation. It is worth to mentioning that uniform pollutant (tracer gas) emission rate in a room or urban volume is not realistic condition, but they are confirmed to be effectively applied in tracer gas technique to provide ventilation information for both indoor [41,56-59] and outdoor [5, 7-9, 12-14].

In this paper we used uniform tracer gas source from ground up to 2m for ventilation analysis. Fig. 3 shows uniform tracer gas sources (of carbon monoxide CO) nin Group I (Fig. 3a-3b) and Group II (Fig. 3c). The tracer gas emission rate S_c was set to 10^{-7}kg-m^{-3}s^{-1} to ensure the source release produced little disturbance to the flow [5, 7-8].

The governing equation of time-averaged tracer gas (pollutant) concentration ($\bar{c}$) is:

$$\bar{u}_j \frac{\partial \bar{c}}{\partial x_j} - \frac{\partial}{\partial x_j}\left(K_c \frac{\partial \bar{c}}{\partial x_j}\right) = S_c \tag{3}$$

where $\bar{u}_j$ are the velocity components ($\bar{u}, \bar{v}, \bar{w}$) in x, y and z directions, K_c is the turbulent diffusivity of tracer gas. Here $K_c = \nu_t / S_{ct}$, ν_t is the kinematic eddy viscosity and S_{ct} is the turbulent Schmidt number (S_{ct}=0.7) [5, 7-8, 13-14].

For boundary conditions of Eq. (3), the inflow tracer gas concentration was set zero at domain inlet, zero normal flux condition was used at wall surfaces and zero normal gradient condition was applied at domain roof and outlet.

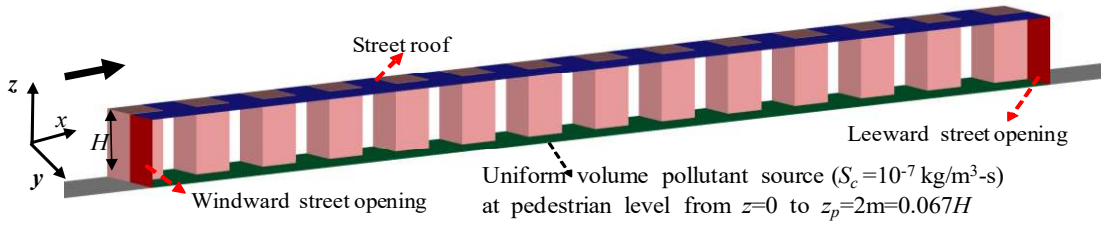

(a)

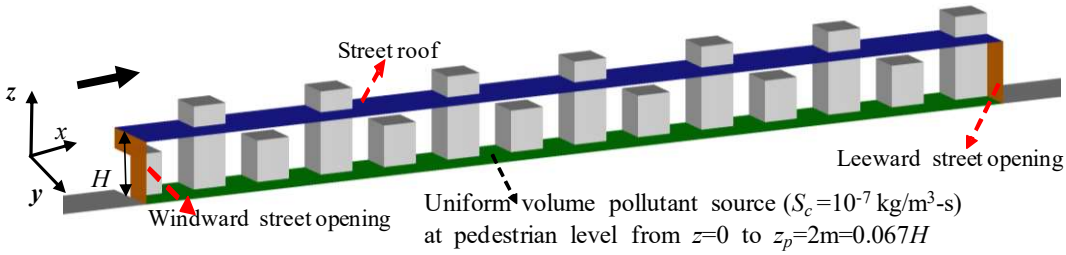

(b)

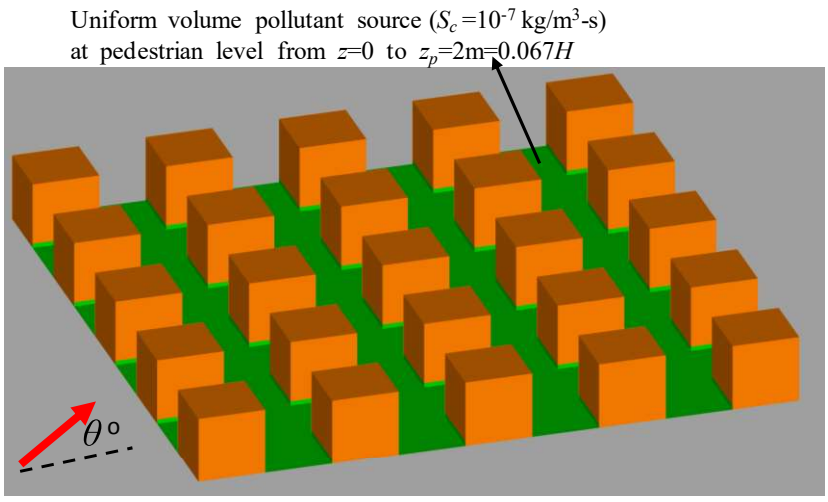

(c)

Fig. 3. Uniform tracer gas (pollutant) source at pedestrian level in cases (a) with uniform heights, (b) with building height variations, (c) with lateral UCL boundaries.

Pollutant transport rates (PTR) and their ratios (CR):

Pollutant dispersion in 2D street canyons always includes two processes, i.e. the ground-level pollutants being mixed in canyons by vortices, then being removed out or re-entering 2D

canyons across canyon roofs. Because pollutant concentration below the street roofs is higher than that above it, vertical turbulent diffusion always helps pollutant removal. Li et al. [21] and Liu et al. [22] reported that turbulent diffusion contributes the major fraction to pollutant removal in 2D deep street canyon. In fact although mean flows can remove pollutant out, they also transport pollutant into the street. Such pollutant re-entry effect reduces the contribution of vertical mean flows in pollutant removal.

Realistic urban areas are three-dimensional (3D) consisting of buildings and street networks with a macroscopic interface (open street roof) from its above layers. Pollutant dispersion in 3D urban areas is due to three processes: pollutants being mixed and redistributed within urban areas, pollutants being diluted by horizontal mean flows flushing urban areas and removed across street openings, pollutants being vertically removed out or re-entering through canopy roofs by vertical mean flows and turbulent diffusion. In 3D neighbourhood-scale urban areas, the area of open urban roof is much greater than the street openings (see the below figure).Turbulent diffusion across urban open roof significantly contribute to removing pollutant released from the ground level [7]. To quantify the process of pollutant removal in 3D urban models, pollutant fluxes due to mean flows (F_m) and turbulent diffusion (F_t) across UCL boundaries were defined [7].

$$F_m = \overline{\vec{V}} \bullet \overline{\vec{n}}\,\overline{c} \tag{4}$$

$$F_t = -K_c \frac{\partial \overline{c}}{\partial n} \tag{5}$$

where $\vec{V}$ is the velocity vector, $\vec{n}$ is the normal unit vector to street openings or UCL roofs.

Then the normalized pollutant transport rates (*PTR*) due to mean flows (FA_m^*) and turbulent diffusion across entire UCL roof (FA_t^*) were also defined [7].

$$FA_m^* = \int F_m dA / \dot{M}_0 = \int \overline{\vec{V}} \bullet \overline{\vec{n}}\,\overline{c} dA / \dot{M}_0 \tag{6a}$$

$$FA_{m\ roof}^*(in) = \int_A \left|\overline{w}(-)\right| \times \overline{c} dA / \dot{M}_0 = \int_A \left| \frac{\overline{w} - \left|\overline{w}\right|}{2} \right| \times \overline{c} dA / \dot{M}_0 \tag{6b}$$

$$FA_{m\ roof}^*(out) = -\int_A \left|\overline{w}(+)\right| \times \overline{c} dA / \dot{M}_0 = -\int_A \left| \frac{\overline{w} + \left|\overline{w}\right|}{2} \right| \times \overline{c} dA / \dot{M}_0 \tag{6c}$$

$$FA_t^* = \int F_t dA / \dot{M}_0 = \int -K_c \frac{\partial \overline{c}}{\partial n} dA / \dot{M}_0 \tag{7}$$

where A is the total area of street openings or entire UCL roof.

Note that pollutant re-entry occurs across some street openings and UCL roof. Here positive *PTR* denotes pollutant re-entering UCL and negative one represents pollutant being removed out. Note that in Eqs. (6-7) the total pollutant emission rate in Case [7-N, 30-30, 0] (i.e. $\dot{M}_0$) was used to normalize *PTR* in all the test cases. If $\dot{M}$ is the actual total pollutant emission rate in each case and it can be normalized as $\dot{M}/\dot{M}_0$ (see Table 1). Obviously the sum of *PTR* across all UCL boundaries equals to $\dot{M}/\dot{M}_0$ in each case.

The contribution ratios are also defined as below.

$$CR_m = \int F_m dA / \dot{M} = \int \vec{V} \bullet \vec{n}\bar{c} dA / \dot{M} \tag{8}$$

$$CR_t = \int F_t dA / \dot{M} = \int -K_c \frac{\partial \bar{c}}{\partial n} dA / \dot{M} \tag{9}$$

Similarly the sum of *CR* across all UCL boundaries is 100%.

Pedestrian purging flow rate (PFR) and net escape velocity (NEV):

The concept of purging flow rate (*PFR*) was first introduced by Sandberg and Sjöberg [56] to assess the effective airflow rate of flushing the whole room induced by the convection (i.e. mean flows) and turbulent diffusion. *PFR* was defined as the ratio of pollutant generate rate to the average pollutant concentration in the room. Later, *PFR* was used for estimating the net capacity of removing pollutant in urban domain [5, 7]. If a uniform contaminant source (here S_c=10^{-7} kgm^{-3}s^{-1}) is fixed in the entire pedestrian volume (*Vol, z*=0 to 2m, see Fig. 3), the pedestrian purging flow rate (PFR_{ped}, m^3/s) is as below:

$$PFR_{ped} = \frac{S_c \times Vol}{< C >_{ped}} = \frac{S_c \times Vol}{\int_{Vol} C dx dy dz / Vol} \tag{10}$$

Here $< C >_{\text{ped}}$ is the spatially-averaged concentration in the entire pedestrian air volume (*Vol*).

However *PFR* has the dimension of airflow rate and thus is usually dependent on the volume size of the target domain, i.e. a bigger target domain tends to attain greater *PFR*.

Then Lim et al. [40] proposed the concept of net escape velocity (*NEV*) which is the velocity corresponding to the purging flow rate. Thus this paper adopts the net escape velocity for the entire pedestrian volume (NEV_{ped}) and its normalized value (NEV_{ped}*) to assess the net pedestrian-level pollutant dilution.

$$PFR_{ped} = NEV_{ped} \times A_p \tag{11a}$$

$$NEV_{ped}^{*}=NEV_{ped}/U_H \tag{11b}$$

Here A_p is the entire area of boundaries for the entire pedestrian volume in urban areas, U_H=3m/s is the reference velocity at $z=H$ in the upstream free flow (see Eq. (1a)).

Obviously NEV_{ped} represents the net capacity of removing/diluting pollutant from the entire pedestrian level by both mean flows and turbulent diffusion, meanwhile it is independent of the target control volume.

3. Results and discussion

3.1 Validation of CFD flow simulations

Yoshie et al. [43] reported that modified k–ε models, such as the RNG, are able to correct the drawback of the standard k–ε model that severely over-predicts turbulence kinetic energy in separated flows around front corners of buildings. However, they fail in predicting the size of reattachment length behind buildings and under-predict the velocity in weak wind regions. To validate our simulations, we compared wind tunnel data and CFD results in the CFD validation case (Case [7-N, 30-30, 0]), including $\overline{u}(z)$ (stream-wise velocity), $\overline{w}(z)$ (vertical velocity), k(z) (turbulence kinetic energy) at Point V1 and $\overline{u}(z)$ at Point V3, as some examples (Fig. 4). The figure shows that the standard k-ε model better predicted $\overline{u}(z)$ and $\overline{w}(z)$ than the RNG k-ε model, which usually over-predicted velocity at Points V1 and V3. Both models only predicted the shape of $k(z)$ generally well. These findings are consistent with those by Yoshie et al. [43]. In addition, the coarse grid tended to over-predict $\overline{u}(z)$ and $\overline{w}(z)$. Although there are a little difference between the medium grid and fine grid, both of them predicted the velocity profiles generally well except that the medium grid did a little better at Point V1 than the fine grid.

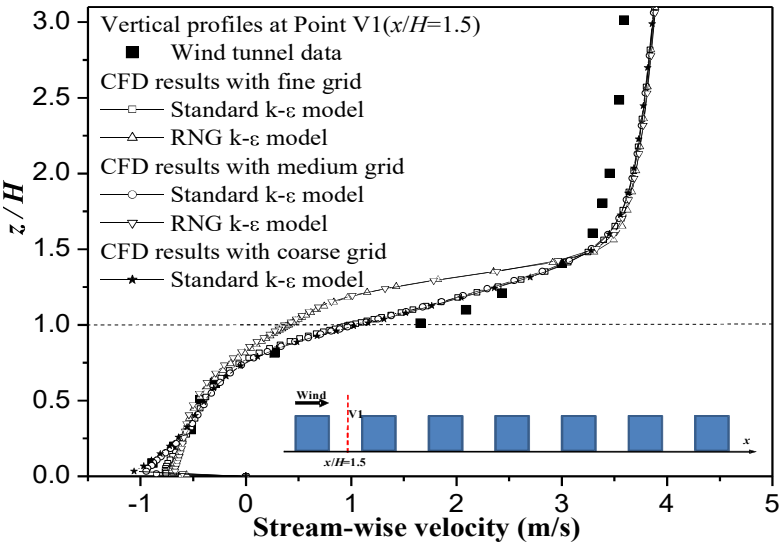
Vertical profiles at Point V1(x/H=1.5)
Wind tunnel data
CFD results with fine grid
Standard k-ε model
RNG k-ε model
CFD results with medium grid
Standard k-ε model
RNG k-ε model
CFD results with coarse grid
Standard k-ε model
z / H
Stream-wise velocity (m/s)
Wind
V1
x/H=1.5
x

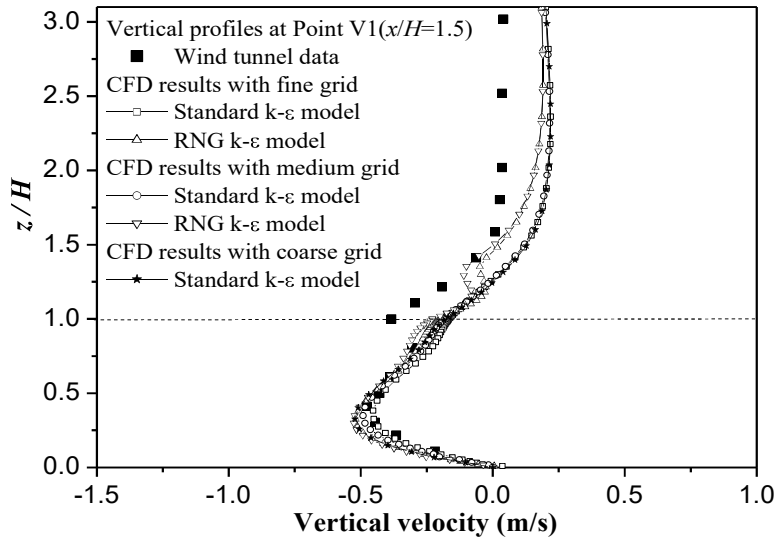
Vertical profiles at Point V1(x/H=1.5)
Wind tunnel data
CFD results with fine grid
Standard k-ε model
RNG k-ε model
CFD results with medium grid
Standard k-ε model
RNG k-ε model
CFD results with coarse grid
Standard k-ε model
z / H
Vertical velocity (m/s)

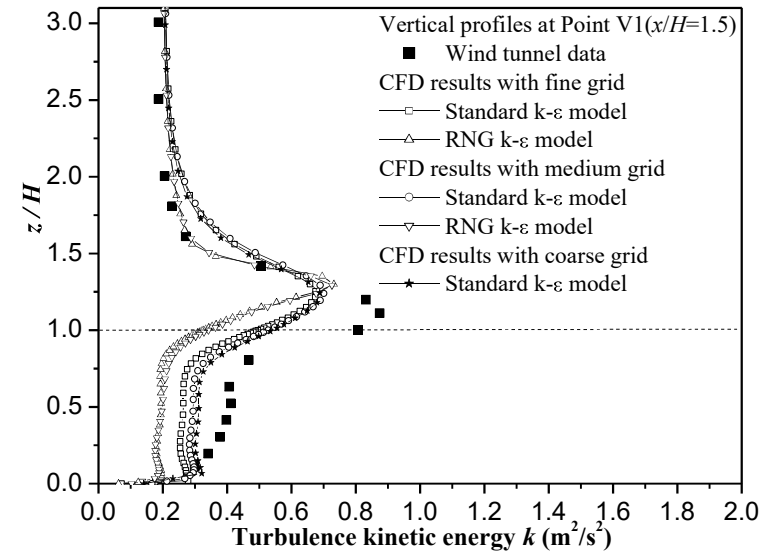
Vertical profiles at Point V1(x/H=1.5)
Wind tunnel data
CFD results with fine grid
Standard k-ε model
RNG k-ε model
CFD results with medium grid
Standard k-ε model
RNG k-ε model
CFD results with coarse grid
Standard k-ε model
z / H
Turbulence kinetic energy k (m²/s²)

(a)

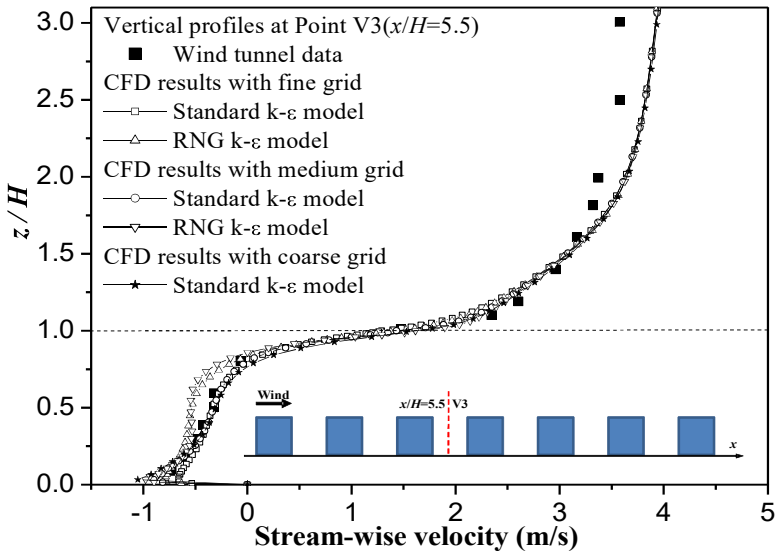

(b)

Fig. 4. Vertical profiles in Case [7-N,30-30,0] (experimental data and CFD results): (a) $\overline{u}(z)$, $\overline{w}(z)$, k(z) at Point V1, (b) $\overline{u}(z)$ at Point V3.

To assess the overall model performance, several standard metrics have been applied to the flow values measured and calculated at V1, V3 and V5, namely the mean, the standard deviation (st.dev.), the normalized mean square error NMSE, the fraction of predictions within a factor of two of observations FAC2, the fractional bias FB and the correlation coefficient R [51]. We remind here that NMSE and FB make no sense for parameters that can take both positive and negative values, such as velocity components. According to COST Action 732 [51], even though there are not fixed values, recommended criteria may be given by the following values: NMSE $\leq$ 1.5; FAC2 $\geq$ 0.5; $-0.3 \leq$ FB $\leq$ 0.3. Results for the medium grid are presented in Table 2, which shows a quite satisfactory model performance in terms of the essential features of the mean velocity.

Overall considering both the numerical accuracy and the computational time, the standard k-ε model with the medium grid arrangement was selected for all CFD simulations. The grid resolution close to the wall surfaces can be considered appropriate also for the case with uniform wall heating. Recently Santiago et al. [55] employed RANS models to simulate flow for simplified urban configurations (with the same packing density of our cases) with microscale distributions of surface thermal forcing by using a cell resolution equal to H/16, which is even coarser than that used in the present paper. They found the grid resolution equal to H/16 was able to provide results in good agreement with wind tunnel data.

Table 2. Results of the flow statistical analysis.

	WT/Turb. model	Stream-wise vel.			Vertical vel.		TKE	
		V1	V3	V5	V1	V5	V1	V5
Mean	*WT*	1.59	1.47	1.58	-0.21	-0.13	0.42	0.31
	k-ε	1.59	1.54	1.68	-0.13	-0.12	0.37	0.18
	RNG *k-ε*	1.39	1.49	1.68	-0.17	-0.14	0.26	0.14
St dev.	*WT*	1.74	1.74	1.64	0.19	0.06	0.22	0.07
	k-ε	1.73	1.81	1.79	0.17	0.12	0.15	0.05
	RNG *k-ε*	1.86	1.88	1.90	0.26	0.12	0.10	0.04
NMSE	*k-ε*	---	---	---	---	---	0.10	0.36
	RNG *k-ε*	---	---	---	---	---	0.45	0.78
FAC2	*k-ε*	1.00	1.00	0.93	0.44	0.44	1	0.63
	RNG *k-ε*	0.73	0.94	0.93	0.56	0.63	0.88	0.38
FB	*k-ε*	---	---	---	---	---	0.14	0.51
	RNG *k-ε*	---	---	---	---	---	0.48	0.74
R	*k-ε*	0.99	1.00	1.00	0.96	0.78	0.89	0.35
	RNG *k-ε*	0.95	1.00	1.00	0.94	0.81	0.79	-0.04

3.2 Effect of stream-wise urban size *Lx*, building height variations and wall heating (Group I, θ=0°, cfr. Table 1)

3.2.1 Effect of building height variations in isothermal cases

As an example, Fig. 5 shows 3D streamlines, pressure distribution at wall surfaces and $\bar{c}$ in Case [14-N,30-30,0] and Case [14-N,20-40,0]. The wind was strongly blocked by the first buildings, and some air was driven into UCL volume across windward openings. Flowing along the main street, a fraction of air leaved upwardly across UCL roofs due to the form drag by the buildings, and the other fraction flew through UCL for pollutant dilution. With uniform height, 3D helical flows occurred in each secondary street (Fig. 5a) which may bring external air into it to help pollutant dilution, meanwhile producing pollutant re-entry into UCL. However, in the presence of building height variations, taller buildings produced stronger form drag than lower ones, producing downward helical flows in front of the taller buildings and upward helical flows behind them (Fig. 5b). As a consequence, $\bar{c}$ in front of taller buildings was much lower since the downward flows brought relatively clean air (Fig. 5d), differing from that with uniform height (Fig. 5c).

To quantify the above processes, Fig. 6 shows pollutant fluxes induced by mean flows (F_m) and turbulent diffusion (F_t) across street roofs in Case [14-N, 30-30, 0] (Fig. 6a-6b) and Case [14-N, 20-40, 0] (Fig. 6c-6d). Here negative values denote pollutant leaving UCL and positive

ones represent pollutant re-entering UCL. There are both negative and positive F_m across secondary-street roof in Case [14-N, 30-30, 0] (Fig. 6a), however F_m in Case [14-N, 20-40, 0] was mainly negative behind taller buildings (i.e. removing pollutant upwardly) and positive in front of them (i.e. pollutant re-entering downwardly) (Fig. 6c). More importantly, F_t across street roofs was always negative in both cases (Fig. 6b and 6d). This shows turbulent diffusion always contributed to pollutant removal since $\bar{c}$ below UCL roof was usually higher than that above it.

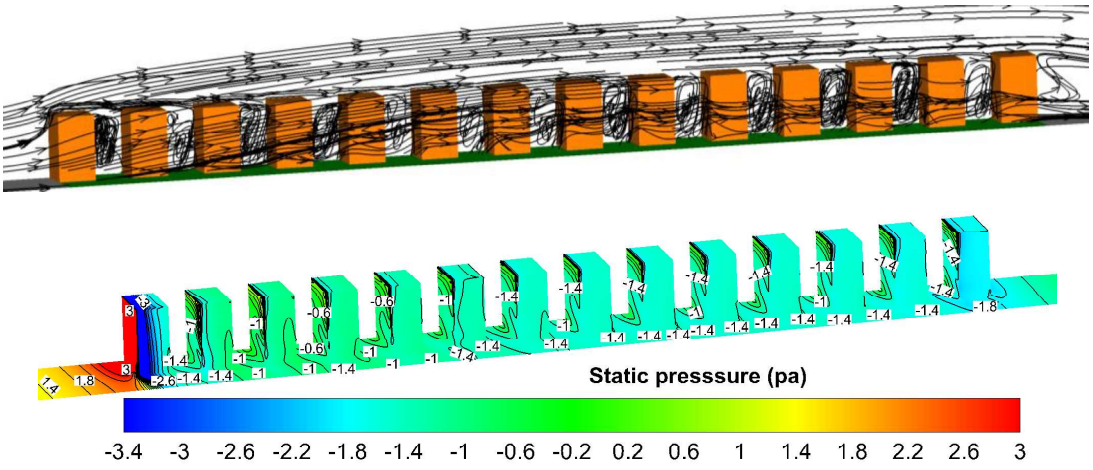

(a)

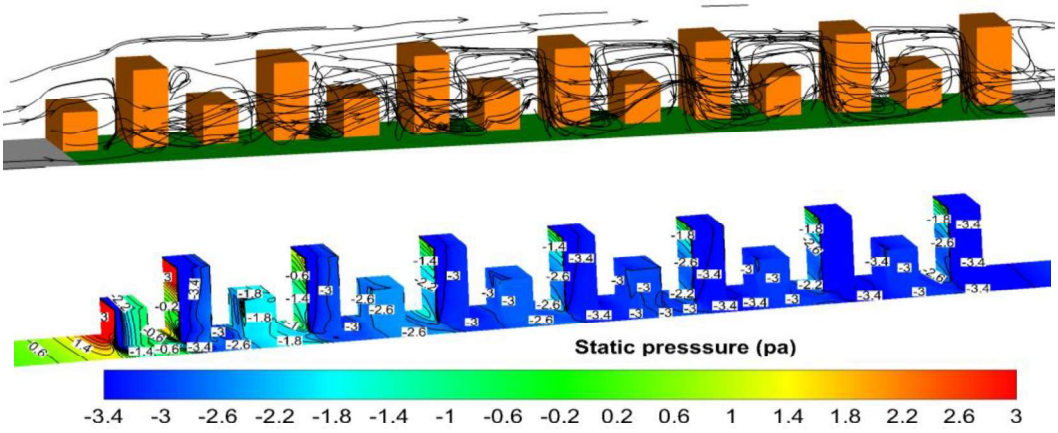

(b)

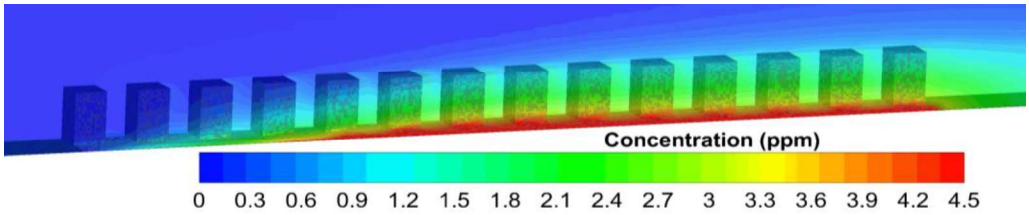

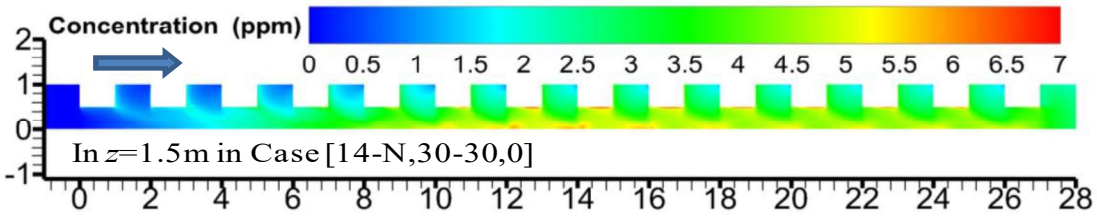

(c)

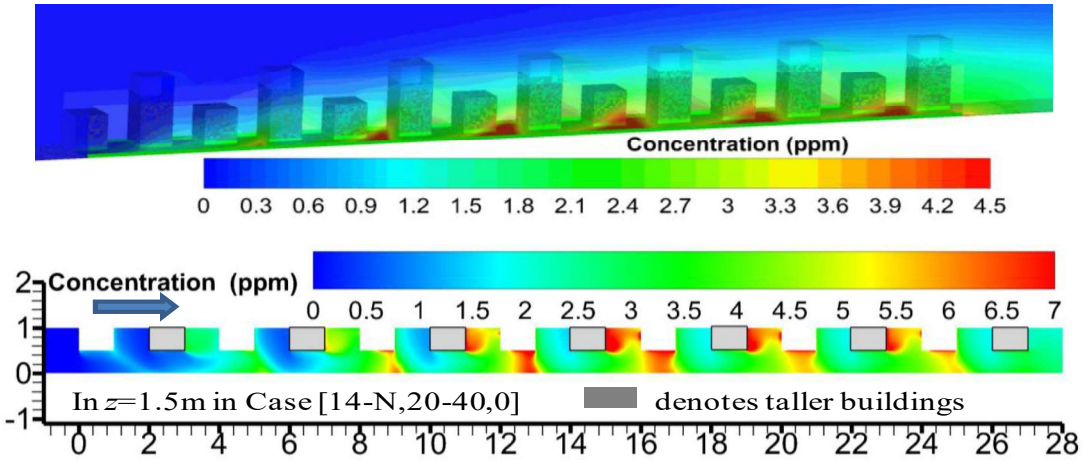

(d)

Fig. 5. Case [14-N,30-30,0] and Case [14-N,20-40,0]: (a-b) 3D streamline and pressure at wall surfaces, (c-d) Pollutant concentration $\bar{c}$.

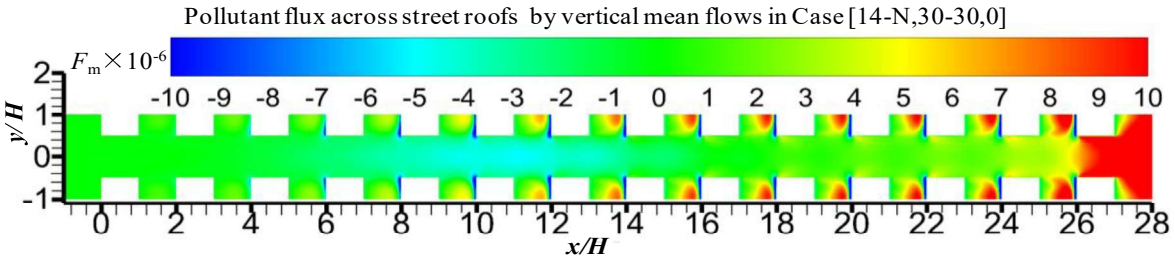

(a)

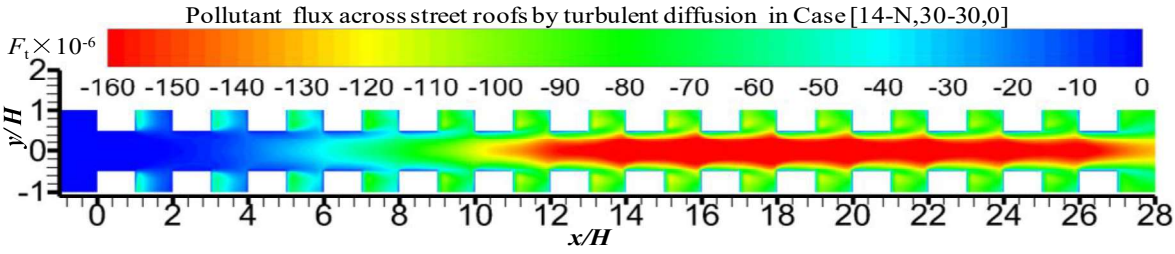

(b)

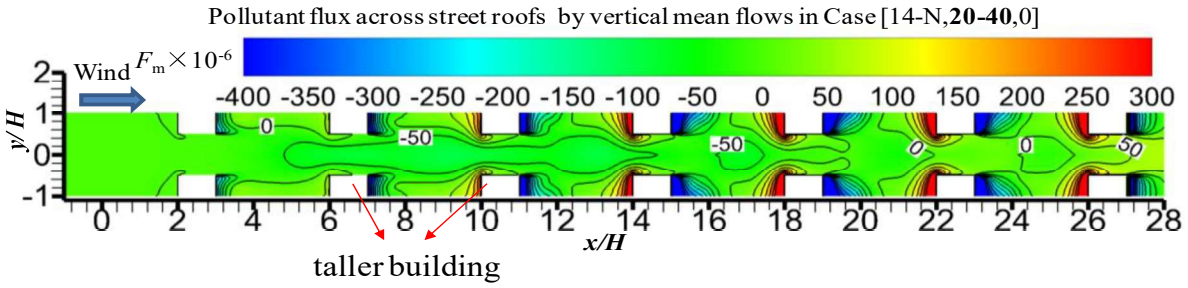

(c)

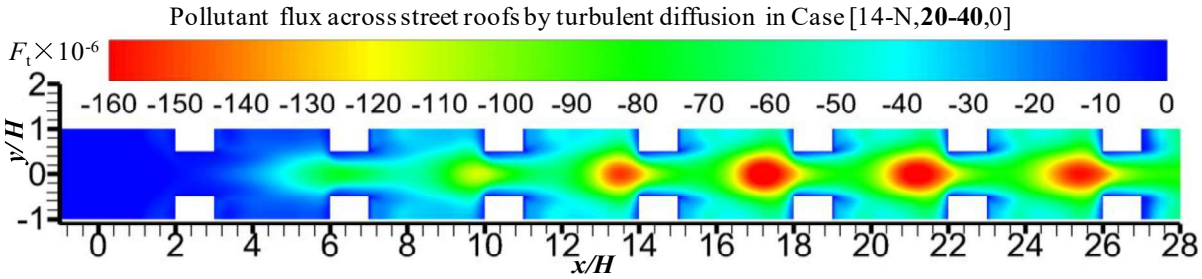

(d)

Fig. 6. F_m and F_t in (a-b) Case [14-N, 30-30, 0], (c-d) Case [14-N, 20-40, 0].

3.2.2 Effect of uniform heating at all wall surfaces

To explain the effect of all wall heating on urban airflows, Fig. 7a-7b show the flow vector at y=H=30m (centre plane of the secondary streets) in Case [28-N,30-30,0] and Case [28-N,20-40,0] with and without wall heating. Obviously, in both cases uniform heating at all wall surfaces enhanced the vortex flow in the secondary streets perpendicular to the approaching wind, as found in the literature [36-37, 54]. Allegrini et al. [35-36] experimentally and numerically confirmed that all wall heating can significantly strengthen recirculation flow in 2D street canyon (H/W=1). Santiago et al. [55] recently verified that wall heating in similar 3D urban-like geometries (H/W=1, λ_p=λ_f=0.25) can increase the velocity below the urban rooftop, especially close to the ground.

Then Fig. 7c-7f display horizontal profiles of $\overline{u}(x)$, $k(x)$ and $\overline{c}(x)$ along the street centerline at z=1.5m and drag coefficient (C_P) for each building. Here $C_P = \dfrac{F_D}{0.5\rho U_H{}^2 A_f}$, where $F_D = \int_0^H \Delta P(z)dz$ is the drag force of each building calculated by pressure difference between windward and leeward building surfaces, U_H=3m/s is the reference velocity, A_f is the frontal area

of one building in Case [28-N,30-30,0]. Note that x/H=0 corresponds to the location of windward street opening. Finally Fig. 8 shows concentration and temperature distribution at z=1.5m=0.05H (pedestrian level).

Looking at the figures it can be noted that for isothermal cases, similar to the findings by Belcher et al. [59], there was an "adjustment region" experiencing a velocity reduction (see Fig. 7c-7d). The starting point was at about x=22H in Case [28-N,30-30,0], which was slightly larger than Case [28-N,20-40,0]. Then a flow balance was established in the interior region [60] or fully-developed region [45] in which the macroscopic flow remains constant (see $\overline{u}(x)$ and $k(x)$ in Fig. 7c-7d). However, due to the pollutant accumulation effect, $\overline{c}$ continued to slightly increase downstream (Fig. 7e). All flow quantities varied following a wave shape (Fig. 7c-7d) due to the flow resistance by buildings (Fig. 7f). The magnitude of such wave-shape variations was obviously greater in Case [28-N,20-40,0] than that in Case [28-N,30-30,0] (Fig. 7c-7f).

As shown in Fig. 7e and Fig. 8a-8b, the effect of uniform wall heating at all wall surfaces (Q_b=100 W/m^2) induced a decrease of $\overline{c}$ with respect to the isothermal case. In particular, Fig. 7a-7d show that it enhanced the vortex flow in the secondary streets and produced greater $\overline{u}(x)$ and $k(x)$ along the main street, thus resulting in stronger capacity of removing pollutant at pedestrian level. The neighbourhood-scale C_p distribution in Fig. 7f confirms that the form drag with all wall heating was much greater than that in the isothermal case because 3D urban airflows were strengthened by wall heating. The adjustment of C_p distribution was consistent with the adjustment of velocity and turbulence. Finally, Fig. 8c illustrates a heat accumulation effect downstream. The temperature in downstream urban areas was about 2-3^{o}C higher than the upstream rural area for such a neighbourhood-scale medium-dense urban area (L=1650 m, U_H=3m/s) with all wall heating (Q_b=100 W/m^2).

Velocity vector in plane of y=30m in Case [28-N,30-30,0] (isothermal case)

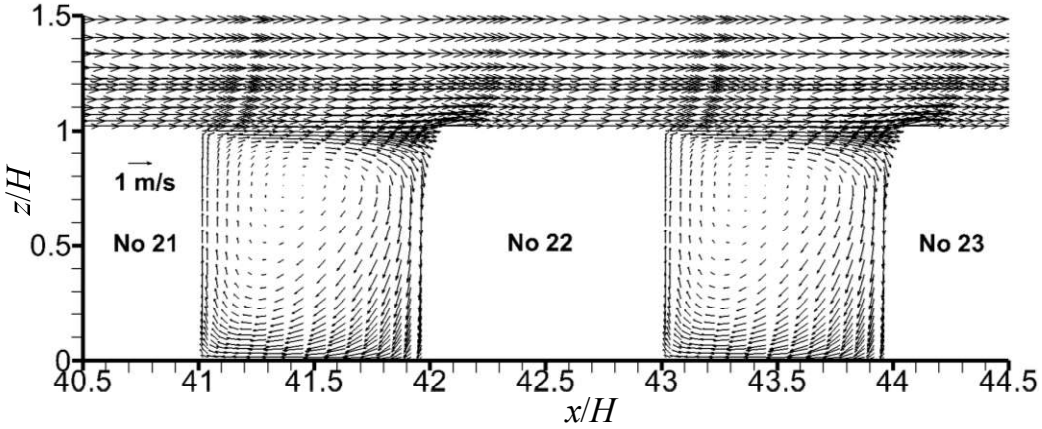

Velocity vector in plane of y=30m in Case [28-N,30-30,0] (with all wall heating)

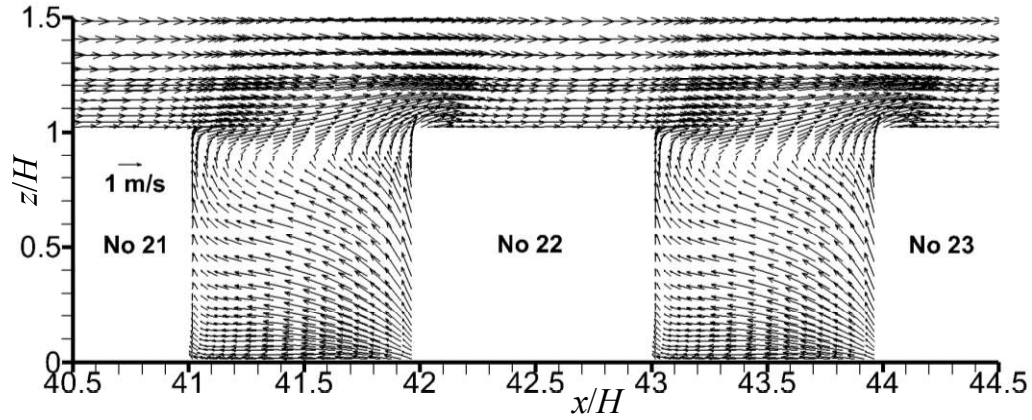

(a)

Velocity vector in plane of y=30m in Case [28-N,20-40,0] (isothermal case)

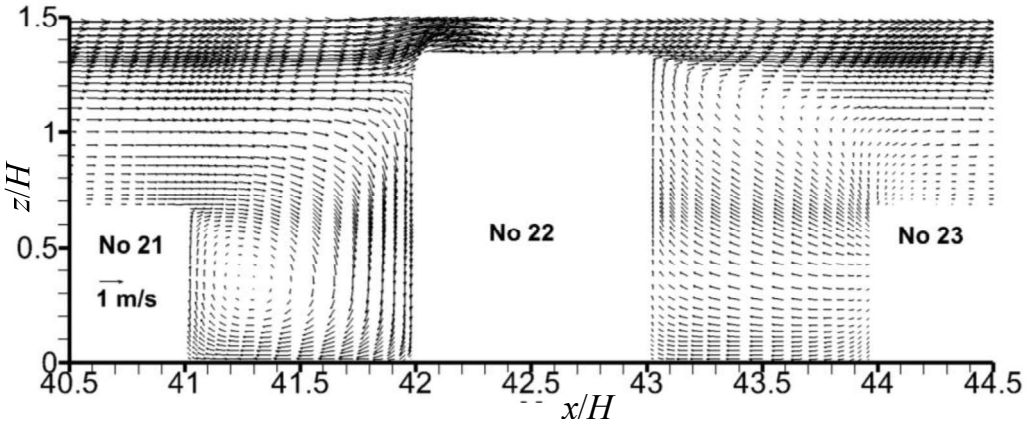

Velocity vector in plane of y=30m in Case [28-N,20-40,0] (with all wall heating)

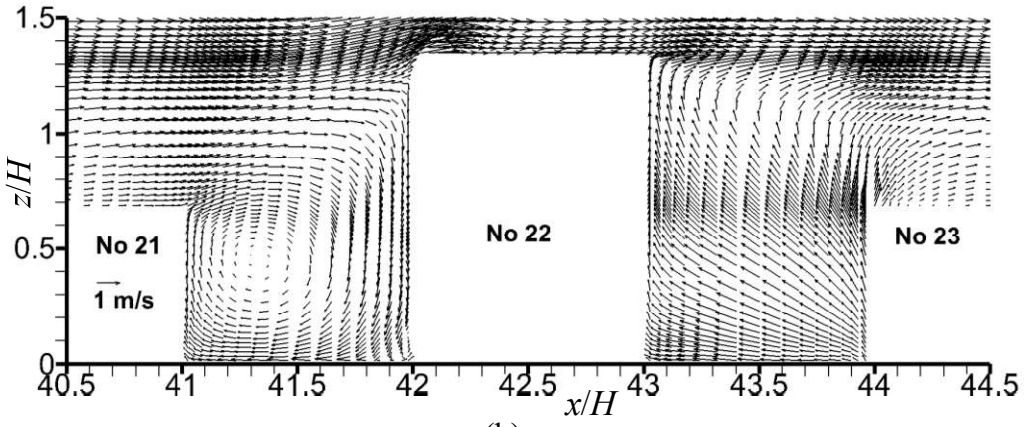

(b)

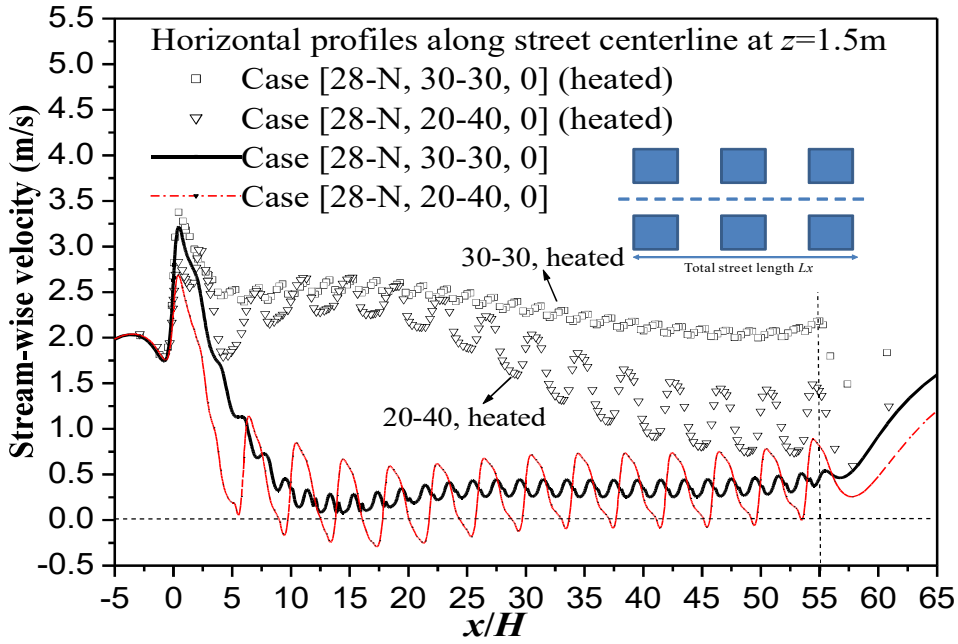

(c)

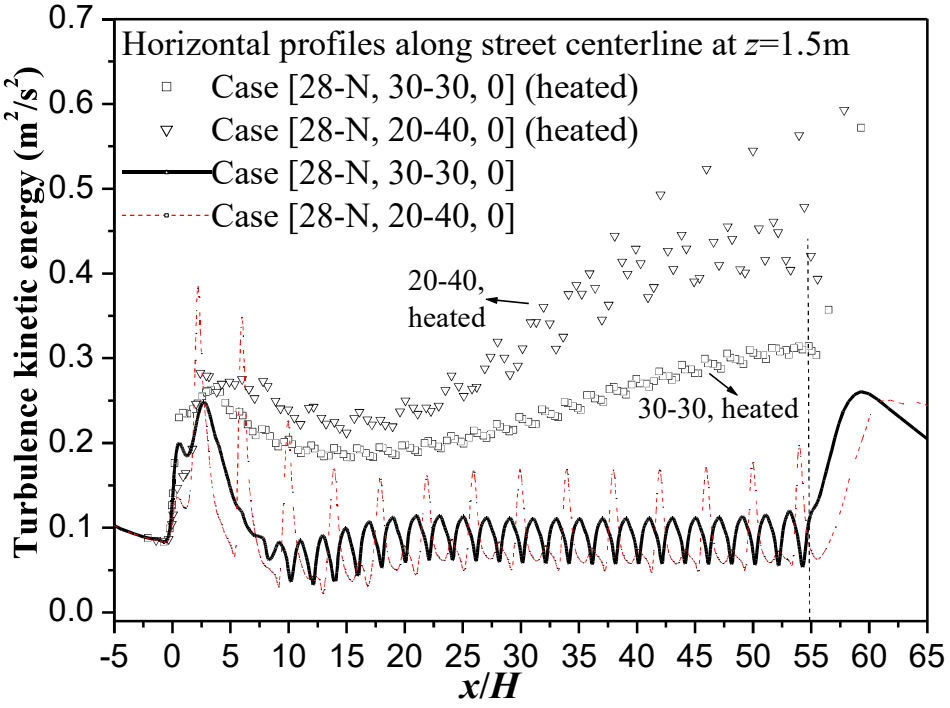
Horizontal profiles along street centerline at z=1.5m
Case [28-N, 30-30, 0] (heated)
Case [28-N, 20-40, 0] (heated)
Case [28-N, 30-30, 0]
Case [28-N, 20-40, 0]
20-40, heated
30-30, heated
Turbulence kinetic energy (m²/s²)
x/H

(d)

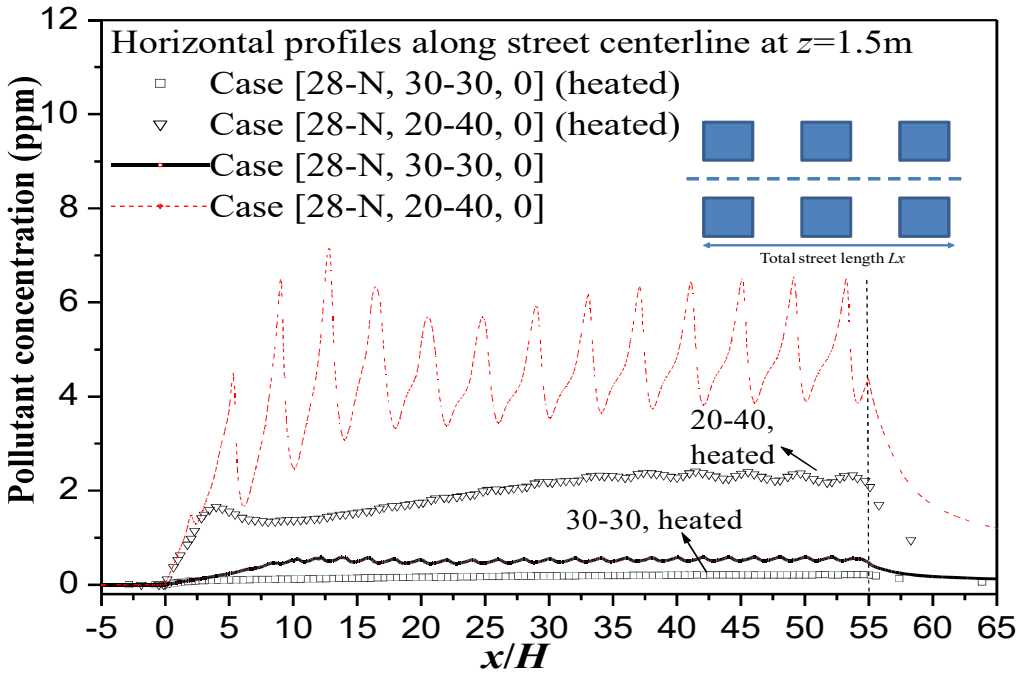
Horizontal profiles along street centerline at z=1.5m
Case [28-N, 30-30, 0] (heated)
Case [28-N, 20-40, 0] (heated)
Case [28-N, 30-30, 0]
Case [28-N, 20-40, 0]
Total street length Lx
20-40, heated
30-30, heated
Pollutant concentration (ppm)
x/H

(e)

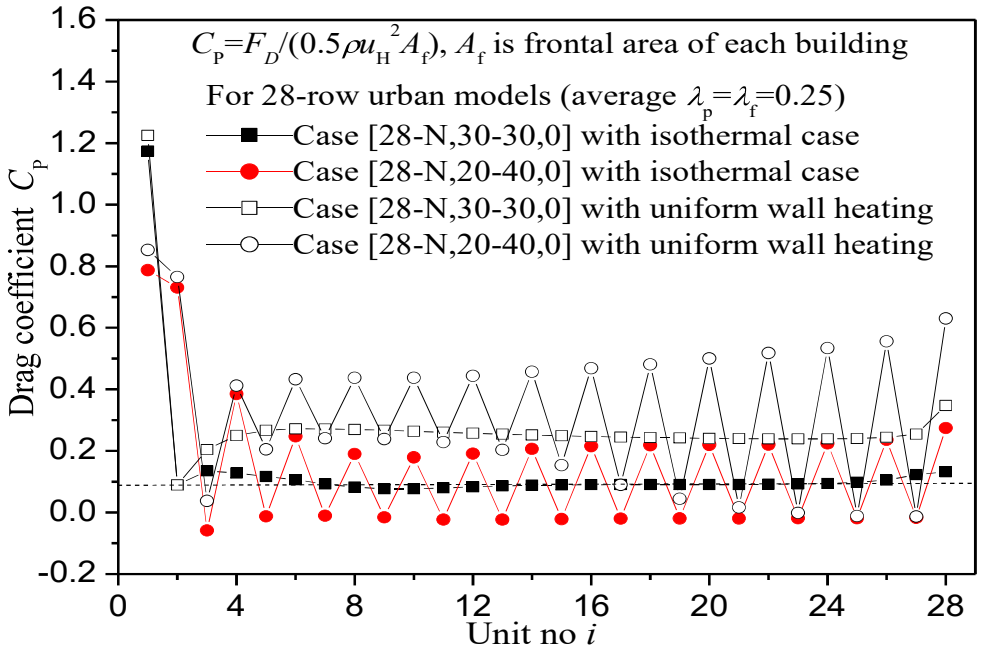

(f)

Fig. 7. In Case [28-N, 30-30, 0] and Case [28-N, 20-40, 0] with uniform wall heating and isothermal condition. (a-b) Velocity vector in plane of y=30m. (c-f) horizontal profiles of $\bar{u}(x)$, $k(x)$, $\bar{c}(x)$ along street centerlines at the height of z=1.5m and drag coefficient (C_p) for each building.

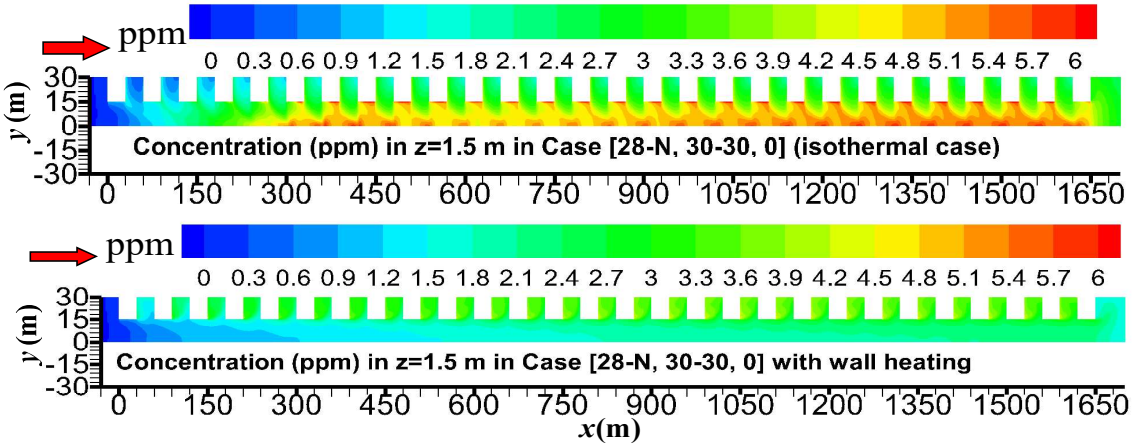

(a)

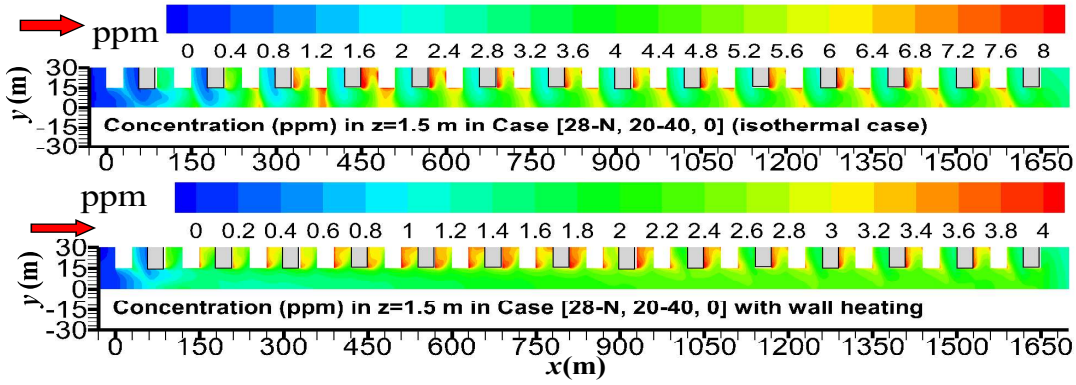

(b)

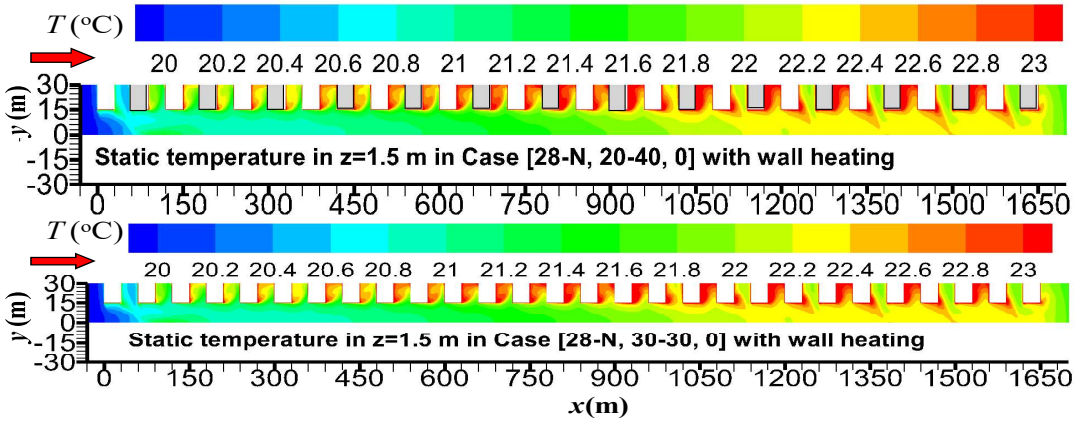

(c)

Fig. 8. At z=1.5m with isothermal condition or wall heating: $\bar{c}$ in (a) Case [28-N, 30-30, 0] and (b) Case [28-N, 20-40, 0]. (c) static temperature at z=1.5m in Case [28-N, 30-30, 0] and Case [28-N, 20-40, 0] with wall heating.

3.2.3 Effect of urban size, building height variations and wall heating on overall PTR/NEV

Fig. 9a-9b shows *PTR* and *CR* in Case [i-N,30-30,0] with a uniform height and various urban size. Negative values denote pollutant is removed out and positive ones represent pollutant re-entry. For street-scale model (i=7, Lx=390m), pollutants were mainly removed out across leeward opening ($FA_m{}^*_{leeward}$=-0.612, its CR_m= 61.2%), while the turbulent counterpart ($FA_m{}^*_{roof}$(turb)=-0.331, CR_t=33.1%) was less important. In neighbourhood-scale models (Lx=810m to 4.17 km), turbulent diffusion was instead much more important for pollutant removal than horizontal mean flows. In fact, $FA_m{}^*_{roof}$(turb) ranged from -1.271 to -9.357 (their *CRs* rise from 63.5% to 89.9%), which was much larger than $FA_m{}^*_{leeward}$=-0.762 to -1.199 (CR=38.1% to 11.5%). Although $FA_m{}^*_{roof}$(out) and $FA_m{}^*_{roof}$(in) were large, their sum was small,

thus vertical mean flows only slightly contributed to pollutant removal due to downward pollutant re-entries. These findings are similar to those found for neighbourhood-scale (~1km) high-rise urban models [7]. Fig. 9c shows that NEV_{ped}* decreased from 0.022 to 0.011 as *Lx* rose from 390m to 4.17km. Thus longer UCL models attained worse pedestrian ventilation due to a pollutant accumulation effect.

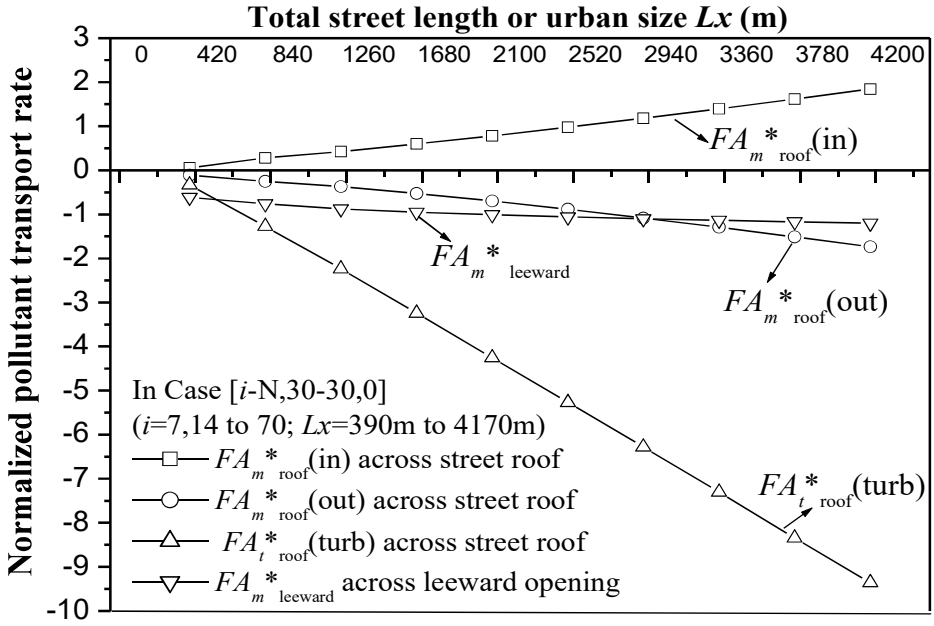

Case [i-N,30-30,0]	FA_m*$_{roof}$ (in)	FA_m*$_{roof}$ (out)	FA_m*$_{roof}$ (turb)	FA_m*$_{leeward}$
Lx = 390m,*i*=7	0.057	-0.112	-0.331	-0.612
Lx =810m,*i*=14	0.282	-0.252	-1.271	-0.762
Lx =1230m,*i*=21	0.425	-0.369	-2.239	-0.878
Lx =1650m,*i*=28	0.599	-0.524	-3.240	-0.952
Lx =2070m,*i*=35	0.783	-0.697	-4.252	-1.010
Lx =2490m,*i*=42	0.978	-0.884	-5.270	-1.058
Lx =2910m,*i*=49	1.182	-1.083	-6.282	-1.099
Lx =3330m,*i*=56	1.395	-1.292	-7.304	-1.136
Lx =3750m,*i*=63	1.616	-1.511	-8.346	-1.169
Lx =4170m,*i*=70	1.845	-1.737	-9.357	-1.199

(a)

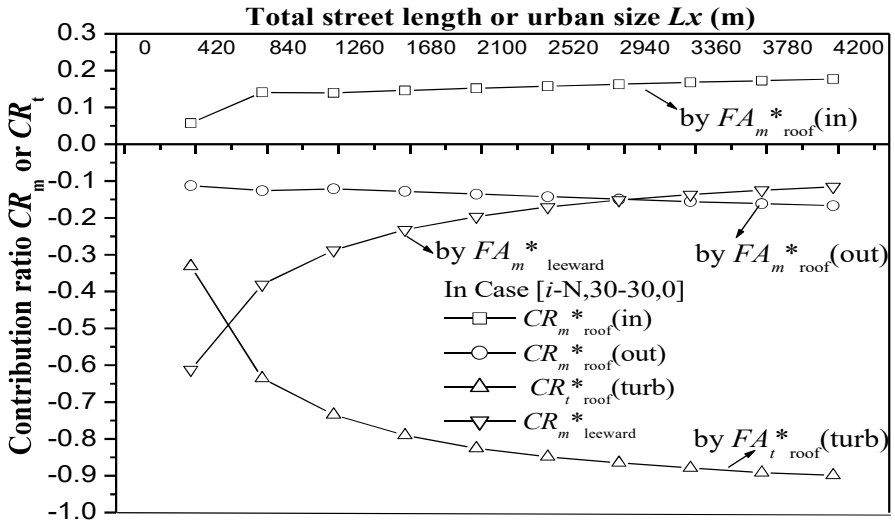

Case [i-N,30-30,0] Contribution ratio of	FA_m*roof (in)	FA_m*roof (out)	FA_m*roof (turb)	FA_m*leeward
Lx = 390m,*i*=7	0.057	-0.112	-0.331	-0.612
Lx =810m,*i*=14	0.141	-0.126	-0.635	-0.381
Lx =1230m,*i*=21	0.139	-0.121	-0.734	-0.288
Lx =1650m,*i*=28	0.146	-0.128	-0.790	-0.232
Lx =2070m,*i*=35	0.152	-0.135	-0.826	-0.196
Lx =2490m,*i*=42	0.157	-0.142	-0.849	-0.170
Lx =2910m,*i*=49	0.163	-0.149	-0.865	-0.151
Lx =3330m,*i*=56	0.168	-0.155	-0.879	-0.137
Lx =3750m,*i*=63	0.173	-0.161	-0.892	-0.125
Lx =4170m,*i*=70	0.177	-0.167	-0.899	-0.115

(b)

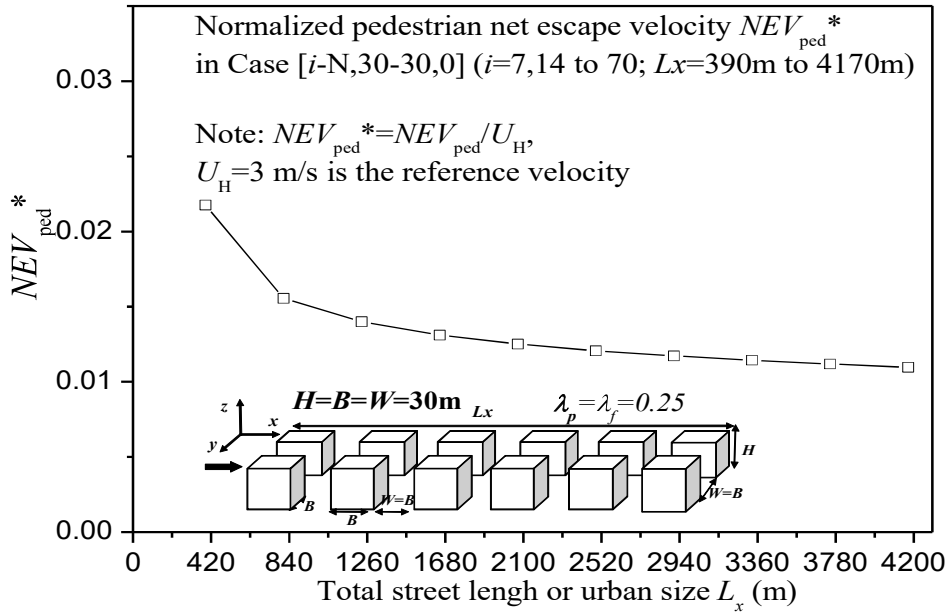

(c)

Fig.9. Case [i-N,30-30,0] (i=7 to 70, Lx=390m to 4170m): (a) PTR and (b) their contribution ratios (CR), (c) NEV_{ped}*.

Fig. 10 shows NEV_{ped}* and PTR in Case [28-N,H1-H2,0] (Lx=1650m) with and without wall heating as σ_H rose from 0% to 83.3%. Since $\dot{M}/\dot{M}_0$ =4.10 was the same for all these 28-row models, CR values are not displayed here. As shown in Fig. 10a it is hard to conclude whether increasing σ_H enhanced or weakened the overall capacity of pollutant removal. However NEV_{ped}* with wall heating (0.022 to 0.024) were much greater than those in isothermal cases (0.012 to 0.013), thus wall heating significantly strengthened pollutant removal at pedestrian level.

For PTR with isothermal condition (see Fig. 10b), as σ_H varied from 0% to 83.3%, FA_m*$_{roof}$ (in) rose from 0.599 to 2.283, FA_m*$_{roof}$(out) increased from -0.524 to -3.649, and their sum changed from 0.075, -0.631 to -1.367. Obviously building height variations enhanced the CR of vertical mean flows. In addition, FA_m*$_{roof}$(turb) and FA_m*$_{leeward}$ slightly decreased from -3.240 to -2.054 and from -0.952 to -0.605. FA_m*$_{roof}$(turb) always contributed more than vertical mean flows. By comparing PTR with and without wall heating, Fig. 10b shows wall heating basically enhanced FA_m*$_{roof}$(turb) and FA_m*$_{roof}$(out), and reduced FA_m*$_{leeward}$. This implies that with wall heating a larger fraction of pollutants was removed out across street roofs vertically, and less pollutant was horizontally purged out across the leeward opening.

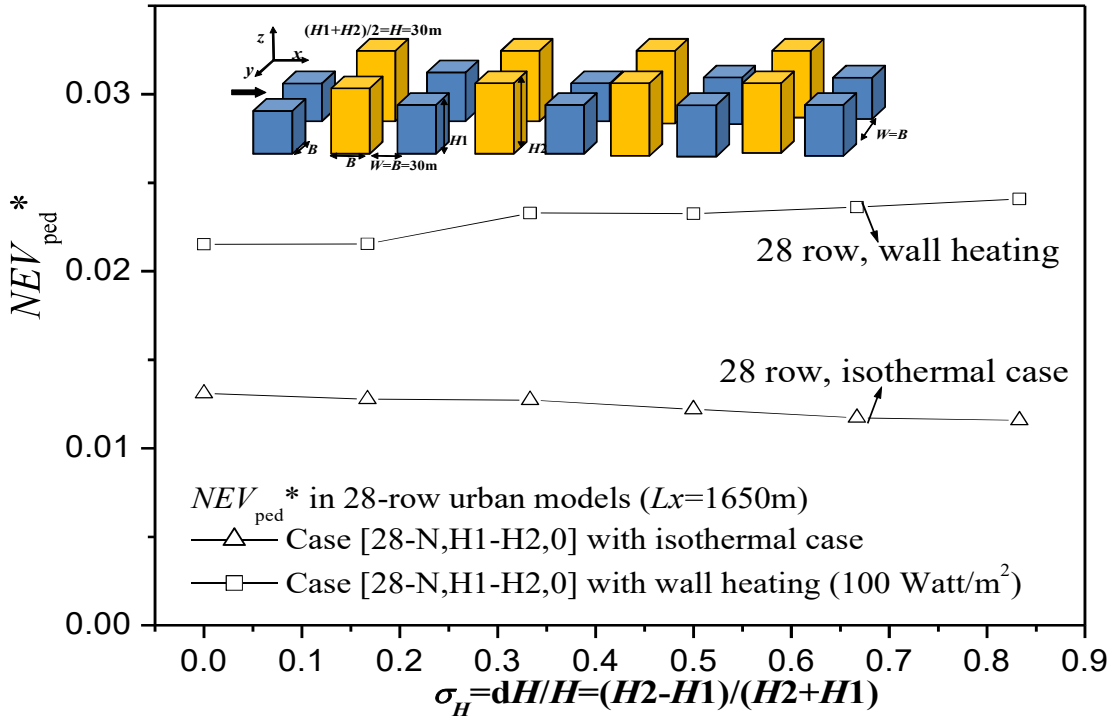
(H1+H2)/2=H=30m
z
x
y
B
H1
H2
W=B
W=B=30m
0.03
0.02
0.01
0.00
NEV ped *
28 row, wall heating
28 row, isothermal case
NEV ped * in 28-row urban models (Lx=1650m)
Case [28-N,H1-H2,0] with isothermal case
Case [28-N,H1-H2,0] with wall heating (100 Watt/m2)
0.0 0.1 0.2 0.3 0.4 0.5 0.6 0.7 0.8 0.9
σH=dH/H=(H2-H1)/(H2+H1)

(a)

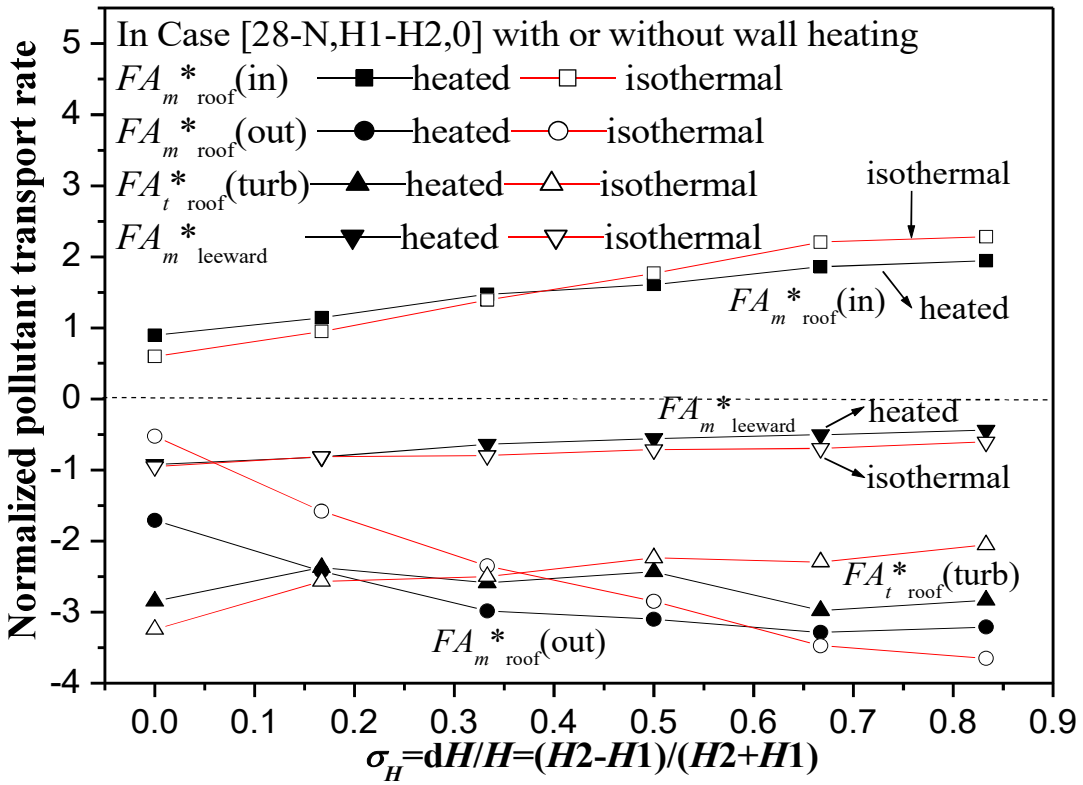
In Case [28-N,H1-H2,0] with or without wall heating
FAm* roof(in) heated isothermal
FAm* roof(out) heated isothermal
FAt* roof(turb) heated isothermal
FAm* leeward heated isothermal
Normalized pollutant transport rate
5 4 3 2 1 0 -1 -2 -3 -4
isothermal
FAm* roof(in)
heated
FAm* leeward
heated
isothermal
FAt* roof(turb)
FAm* roof(out)
0.0 0.1 0.2 0.3 0.4 0.5 0.6 0.7 0.8 0.9
σH=dH/H=(H2-H1)/(H2+H1)

Case [28-N,H1-H2,0]	$FA_m{}^*_{roof}$ (in)	$FA_m{}^*_{roof}$ (out)	$FA_m{}^*_{roof}$ (turb)	$FA_m{}^*_{leeward}$
(Lx =1650m,wall heating)				
$H1$-$H2$=30-30,σ_H=0%	0.895	-1.707	-2.845	-0.921
$H1$-$H2$=25-35,σ_H=16.7%	1.144	-2.421	-2.371	-0.817
$H1$-$H2$=20-40,σ_H=33.3%	1.475	-2.984	-2.587	-0.639
$H1$-$H2$=15-45,σ_H=50.0%	1.611	-3.099	-2.431	-0.558
$H1$-$H2$=10-50,σ_H=66.7%	1.859	-3.283	-2.978	-0.501
$H1$-$H2$=5-55,σ_H=83.3%	1.946	-3.209	-2.832	-0.442
Case [28-N,H1-H2,0]	$FA_m{}^*_{roof}$ (in)	$FA_m{}^*_{roof}$ (out)	$FA_m{}^*_{roof}$ (turb)	$FA_m{}^*_{leeward}$
(Lx =1650m,isothermal)				
$H1$-$H2$=30-30,σ_H=0%	0.599	-0.524	-3.240	-0.952
$H1$-$H2$=25-35,σ_H=16.7%	0.949	-1.580	-2.566	-0.811
$H1$-$H2$=20-40,σ_H=33.3%	1.393	-2.349	-2.495	-0.797
$H1$-$H2$=15-45,σ_H=50.0%	1.769	-2.847	-2.236	-0.712
$H1$-$H2$=10-50,σ_H=66.7%	2.207	-3.471	-2.294	-0.696
$H1$-$H2$=5-55,σ_H=83.3%	2.282	-3.649	-2.054	-0.605

(b)

Fig. 10. Case [28-N,$H1$-$H2$,0] with isothermal condition or wall heating: (a) NEV_{ped}*, (b) PTR.

Summing up, for isothermal cases urban size was found to be the first key parameter for NEV_{ped}*. The longer urban size, the less overall NEV_{ped}* and the more contribution by turbulent diffusion. In contrast to uniform building height, building height variations enhanced PTR by vertical mean flows, but only slightly affected the overall NEV_{ped}*. Building height variations in fact enhanced pollutant removal in secondary streets in front of taller buildings, but also leaded to accumulation in those behind taller buildings. Similarly to 2D street canyon [33-36], uniform wall heating strengthened 3D urban airflows and the overall NEV_{ped}*.

3.3 Effect of urban size and lateral UCL boundaries under a parallel wind (θ=0°)

The above test cases in Group I disregard the effect of lateral UCL boundaries. This subsection takes this effect into account and only considers a parallel wind **(θ=0°)**.

As an example, Fig. 11a shows 3D streamlines and $\bar{c}$ at z=1.5m in Case [9-9,30-30,0]. There were 3D helical flows in the secondary streets and flow channelling along the main street. $\bar{c}$ was higher in downstream and recirculation regions. Across windward openings and street roofs, as well as lateral UCL boundaries, external air entered UCL to help pollutant dilution. Fig. 11b-11c displays PTR and their CR in Case [n-m, 30-30, 0] (n=m=5, 7, 9, 11, Lx=Ly=270m to

630m). FA_m*$_{lateral}$(out) were -0.368 to -0.922, FA_m*$_{lateral}$(in) were 0.141 to 0.786. Moreover FA_m*$_{roof}$ (in) were 0.202 to 3.516 and FA_m*$_{roof}$(out) were -0.581 to -5.604. Their net effects were to remove pollutant out but their *CR* were small (6.6% to 13.3% for FA_m*$_{roof}$,0.4%-4.0% for FA_m*$_{lateral}$) due to a significant pollutant re-entry across them. The major fraction of ground-level pollutants was removed out by FA_m*$_{leeward}$ (*CR*=61.8% to 35.3%) and FA_m*$_{roof}$(turb) (*CR*=23.8% to 58.0%). Fig. 11d shows NEV_{ped}* decreased from 0.027 to 0.018 as urban size rises from 270m to 630m.

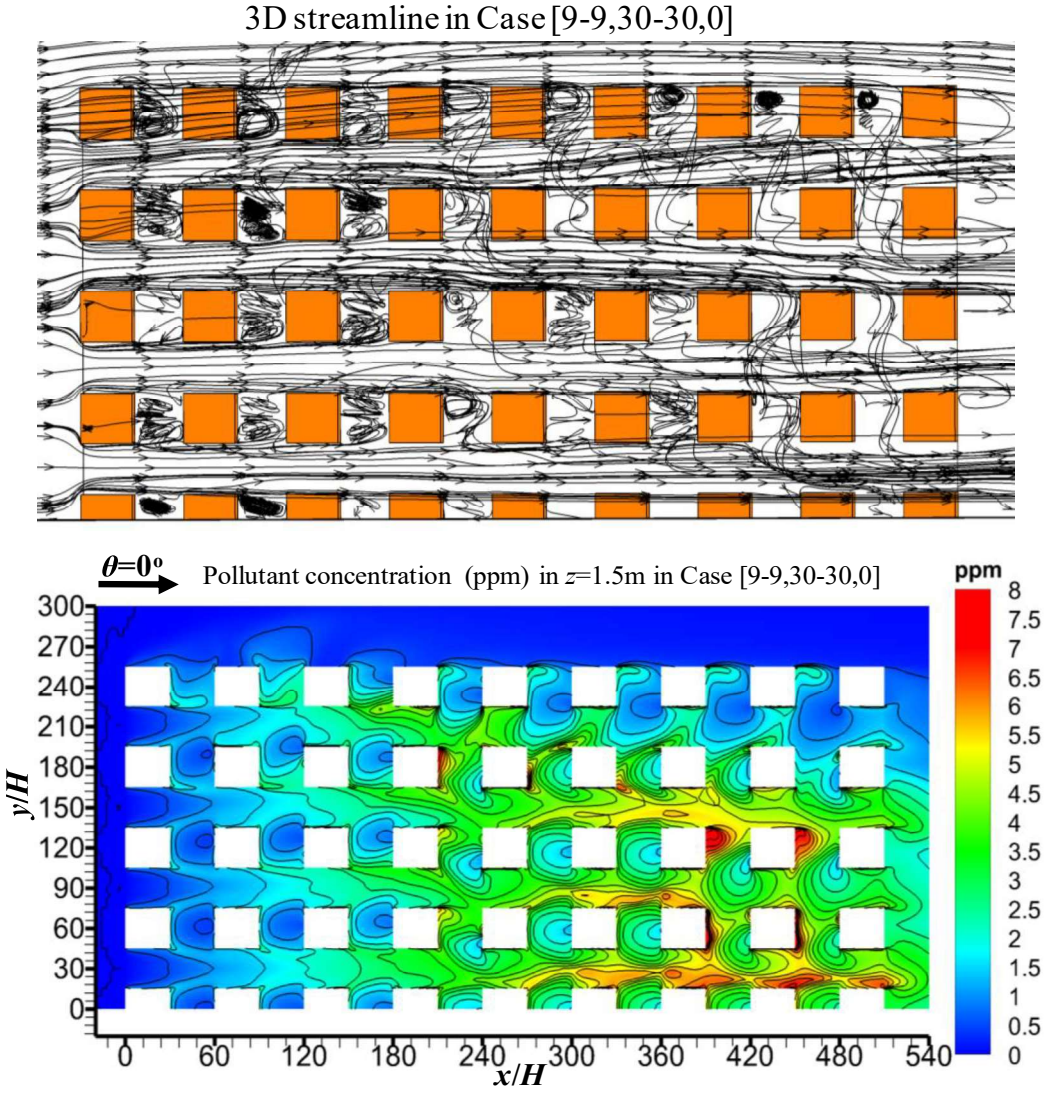

(a)

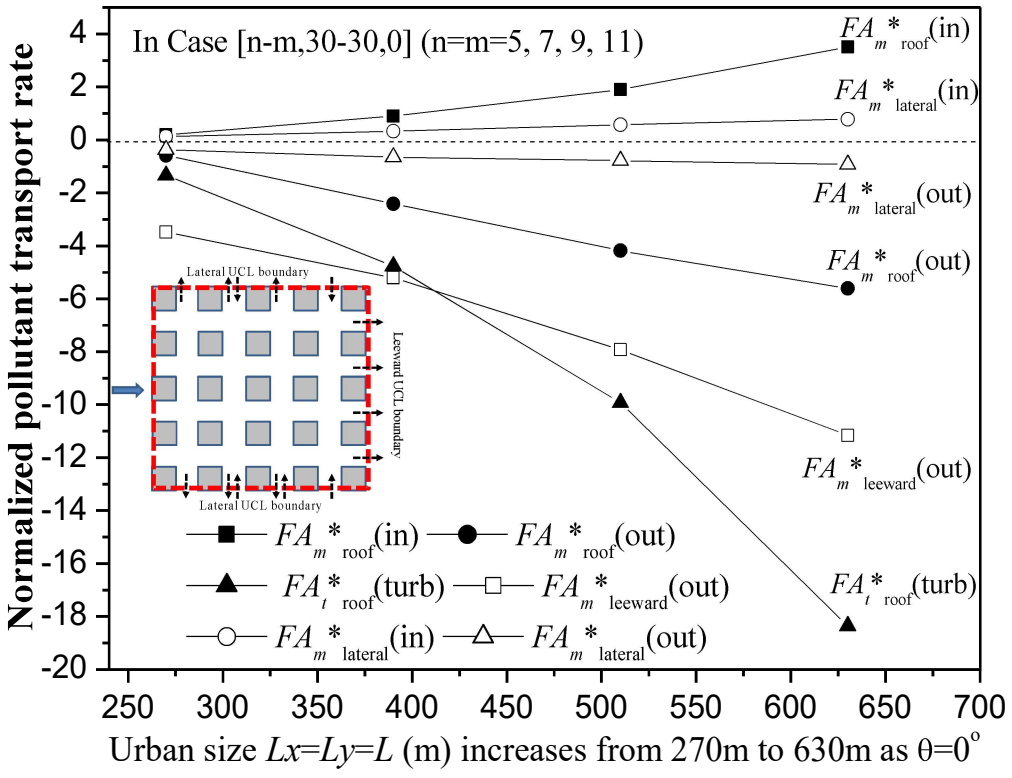
In Case [n-m,30-30,0] (n=m=5, 7, 9, 11)
Normalized pollutant transport rate
Urban size Lx=Ly=L (m) increases from 270m to 630m as θ=0°
Lateral UCL boundary
Leeward UCL boundary
Lateral UCL boundary
FA_m* roof(in)
FA_m* lateral(in)
FA_m* lateral(out)
FA_m* roof(out)
FA_m* leeward(out)
FA_t* roof(turb)
FA_m* roof(in)
FA_m* roof(out)
FA_t* roof(turb)
FA_m* leeward(out)
FA_m* lateral(in)
FA_m* lateral(out)

(b)

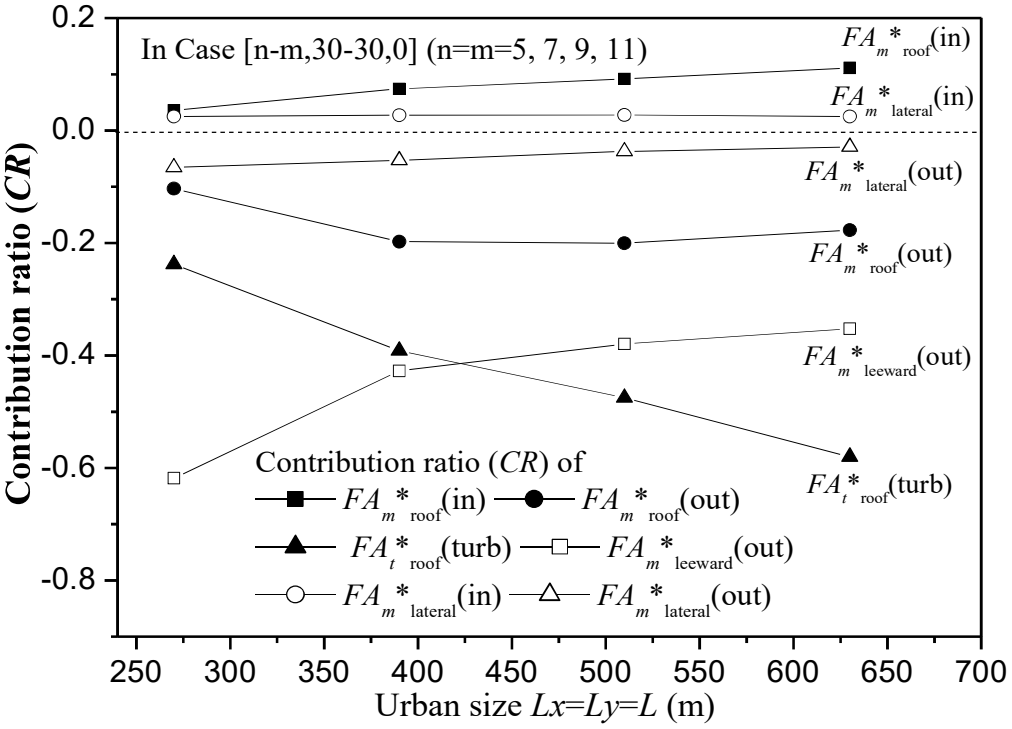
In Case [n-m,30-30,0] (n=m=5, 7, 9, 11)
Contribution ratio (CR)
Urban size Lx=Ly=L (m)
FA_m* roof(in)
FA_m* lateral(in)
FA_m* lateral(out)
FA_m* roof(out)
FA_m* leeward(out)
FA_t* roof(turb)
Contribution ratio (CR) of
FA_m* roof(in)
FA_m* roof(out)
FA_t* roof(turb)
FA_m* leeward(out)
FA_m* lateral(in)
FA_m* lateral(out)

(c)

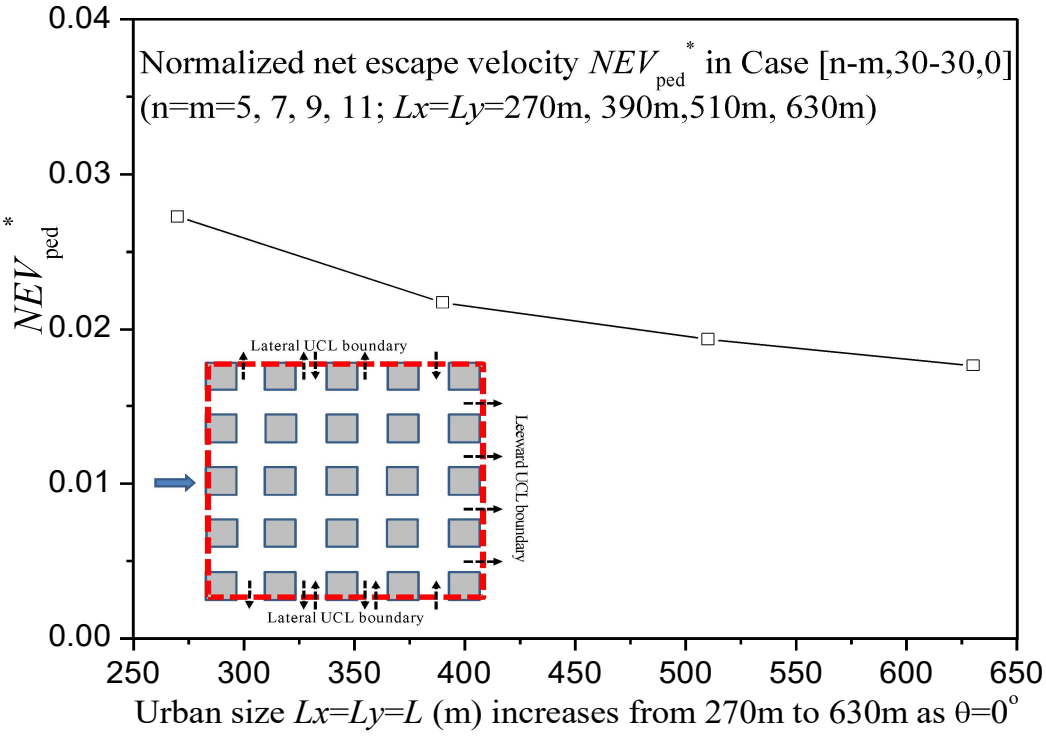

(d)

Fig.11. (a) 3D streamline and $\bar{c}$ at z=1.5m in Case [9-9,30-30,0]. In Case [n-m,30-30,0] (n=m=5, 7, 9, 11): (b-c) *PTR* and their *CR*, (d) NEV_{ped}*.

3.4 Effect of wind direction

Eight test cases, i.e. Case [5-5,30-30,θ] and Case [7-7,30-30,θ] (θ=0°, 15°, 30°, 45°, see Table 1) were investigated. Fig. 12 shows velocity and concentration at z=1.5m in Case [5-5,30-30, θ]. Wind directions was found to be an important factor. Concentration was usually higher in downstream and recirculation regions. Moreover, the parallel approaching wind induced lower concentration than oblique winds.

Fig. 13a-13b show *PTR* and their *CR*. Here FA_m*$_{openings}$ represents the sum of FA_m* across all street openings. Note that, Case [7-7,30-30,θ] and Case[5-5,30-30,θ] are of symmetrical geometry characteristics and θ=-15°, -30°, -45° are theoretically included in the figures.

For Case[5-5, 30-30, θ], as θ changed from 0° to 45°, FA_m*$_{openings}$ ranged from -3.693 to -3.546 (*CR*=65.7% to 63.1%), and FA_m*$_{roof}$(turb) rose from -1.335 to -1.918 (*CR*=23.8% to 34.1%). Obviously FA_m*$_{openings}$ and FA_m*$_{roof}$(turb) constituted the first and second key contribution. Moreover FA_m*$_{roof}$(in) was 0.202 to 0.746 and FA_m*$_{roof}$ (out) was -0.581 to -0.760,

thus their net effect was to remove pollutants out, but their net *CR* were small (0.2% to 13.6%) because pollutant re-entry rates (FA_m*$_{roof}$(in)) were only slightly smaller than FA_m*$_{roof}$(out).

For Case[7-7, 30-30, θ], FA_m*$_{openings}$ were -5.531 to -6.783 (*CR*=45.5% to 55.8%) and FA_m*$_{roof}$(turb) were -4.762 to -5.088 (*CR*=39.2% to 41.8%). Thus FA_m*$_{roof}$ (turb) were as much important as FA_m*$_{openings}$. In addition, FA_m*$_{roof}$(in) were 0.904 to 1.762 and FA_m*$_{roof}$(out) were -2.404 to -1.962. Their net effect only contributed slightly to pollutant removal (*CR*=12.3%(0°), 12.0% (15°), 3.8% (30°), 1.6% (45°)). Finally, Fig. 13c confirms parallel wind (0°) attained the biggest NEV_{ped}* in all these cases.

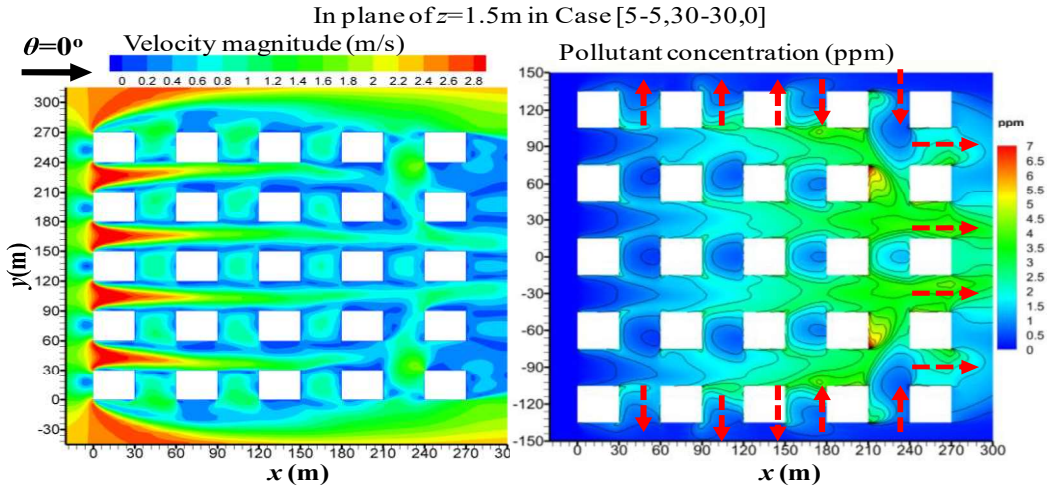

(a)

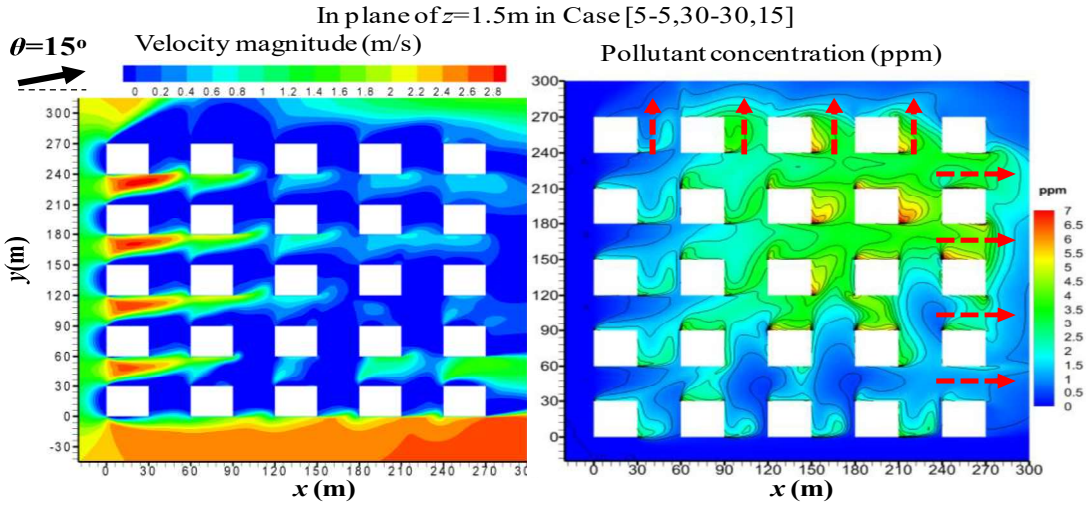

(b)

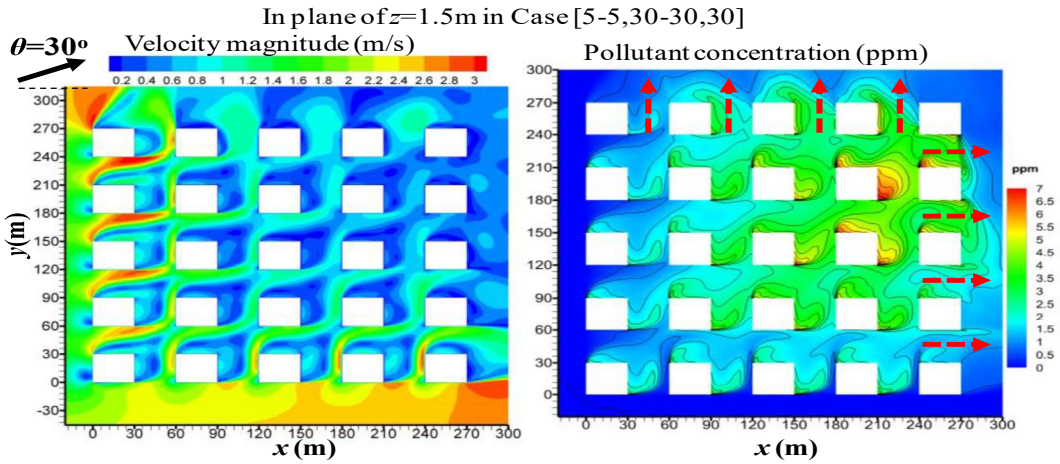

(c)

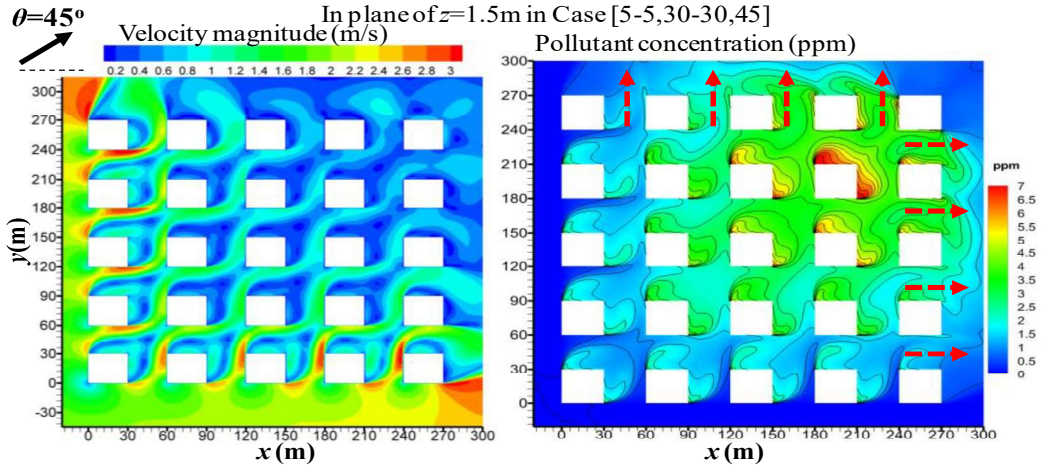

(d)

Fig. 12. Velocity and $\bar{c}$ at z=1.5m in Case [5-5, 30-30, θ]: (a) θ=0°, (b) θ=15°, (c) θ=30°, (d) θ=45°.

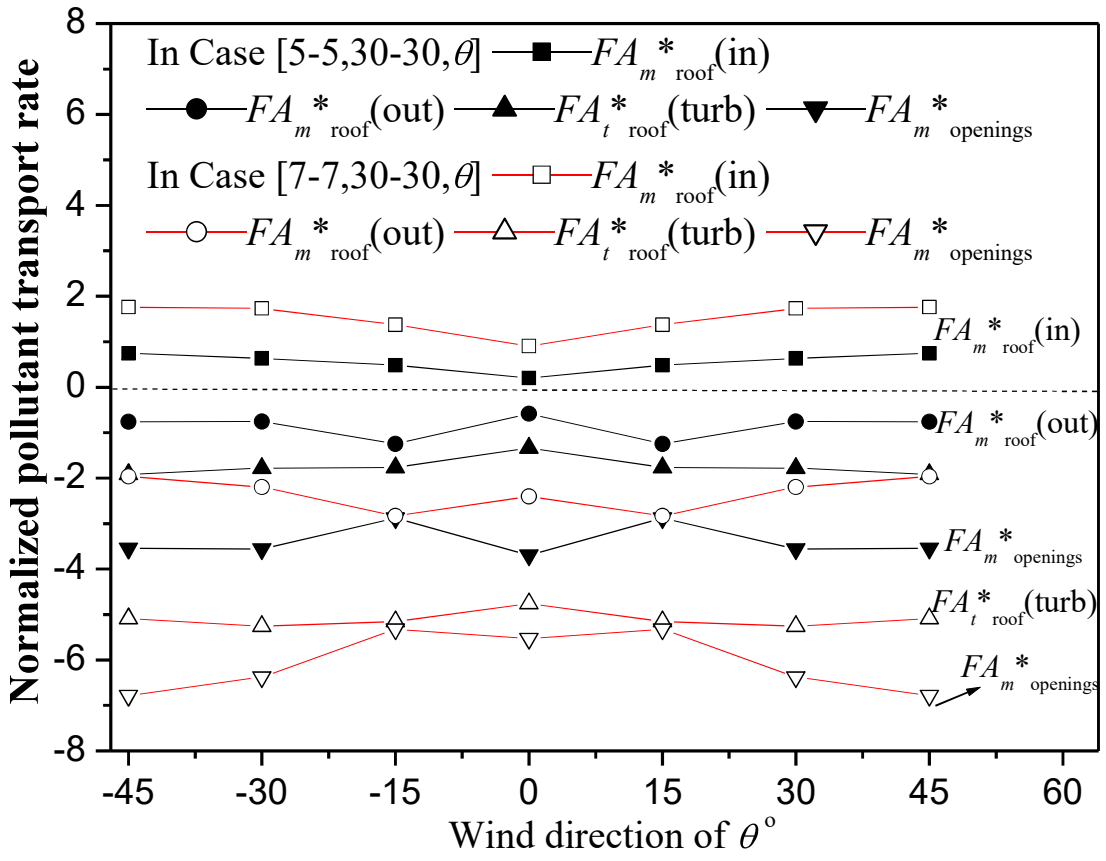

Case [5-5,30-30, θ]	FA_m*$_{roof}$ (in)	FA_m*$_{roof}$ (out)	FA_m*$_{roof}$ (turb)	FA_m*$_{opening}$
Lx =*Ly*=270m				
θ=0°	0.202	-0.581	-1.335	-3.693
θ=15°	0.484	-1.249	-1.765	-2.881
θ=30°	0.636	-0.757	-1.783	-3.560
θ=45°	0.746	-0.760	-1.918	-3.546
Case [7-7,30-30, θ]	FA_m*$_{roof}$ (in)	FA_m*$_{roof}$ (out)	FA_m*$_{roof}$ (turb)	FA_m*$_{opening}$
Lx =*Ly*=390m				
θ=0°	0.904	-2.404	-4.762	-5.531
θ=15°	1.373	-2.831	-5.156	-5.325
θ=30°	1.735	-2.197	-5.259	-6.376
θ=45°	1.762	-1.962	-5.088	-6.783

(a)

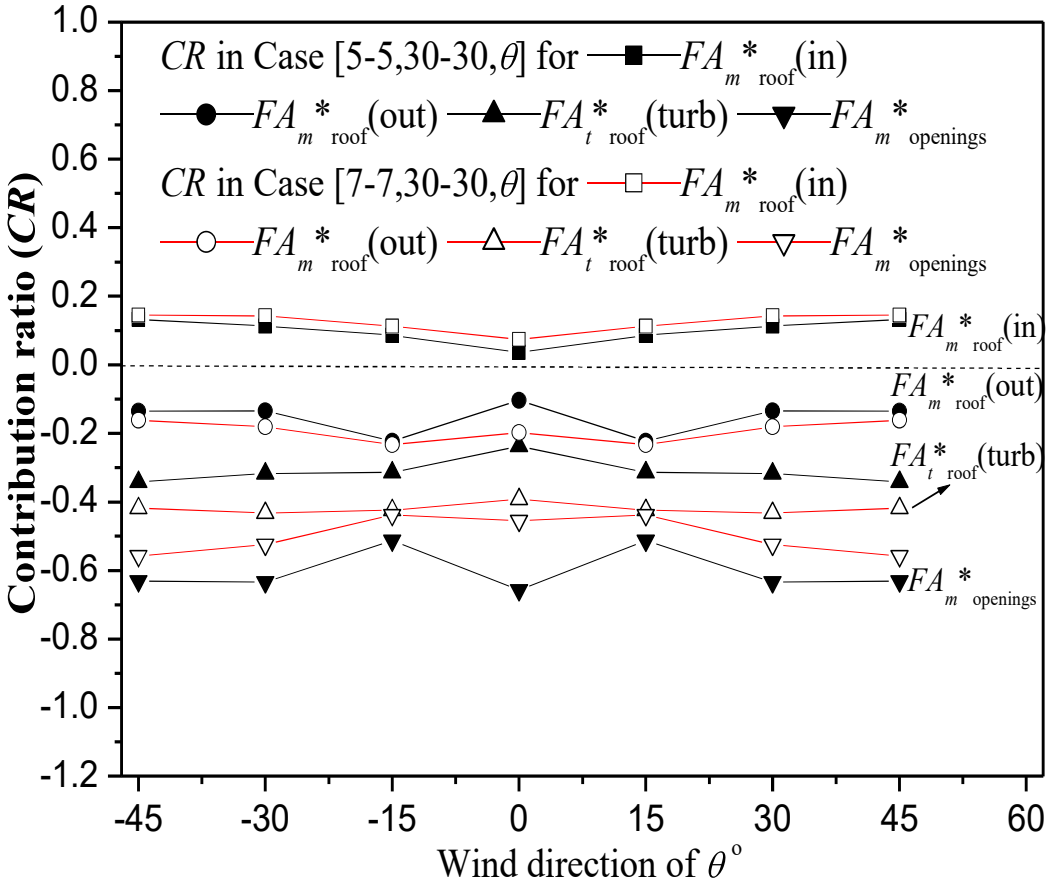

Contribution ratio in Case [5-5,30-30, θ] by	FA_m*$_{roof}$ (in)	FA_m*$_{roof}$ (out)	FA_m*$_{roof}$ (turb)	FA_m*$_{opening}$
θ=0°	0.036	-0.103	-0.238	-0.657
θ=15°	0.086	-0.222	-0.314	-0.513
θ=30°	0.113	-0.135	-0.317	-0.633
θ=45°	0.133	-0.135	-0.341	-0.631
Contribution ratio in Case [7-7,30-30, θ] by	FA_m*$_{roof}$ (in)	FA_m*$_{roof}$ (out)	FA_m*$_{roof}$ (turb)	FA_m*$_{opening}$
θ=0°	0.074	-0.198	-0.392	-0.455
θ=15°	0.113	-0.233	-0.424	-0.438
θ=30°	0.143	-0.181	-0.432	-0.524
θ=45°	0.145	-0.161	-0.418	-0.558

(b)

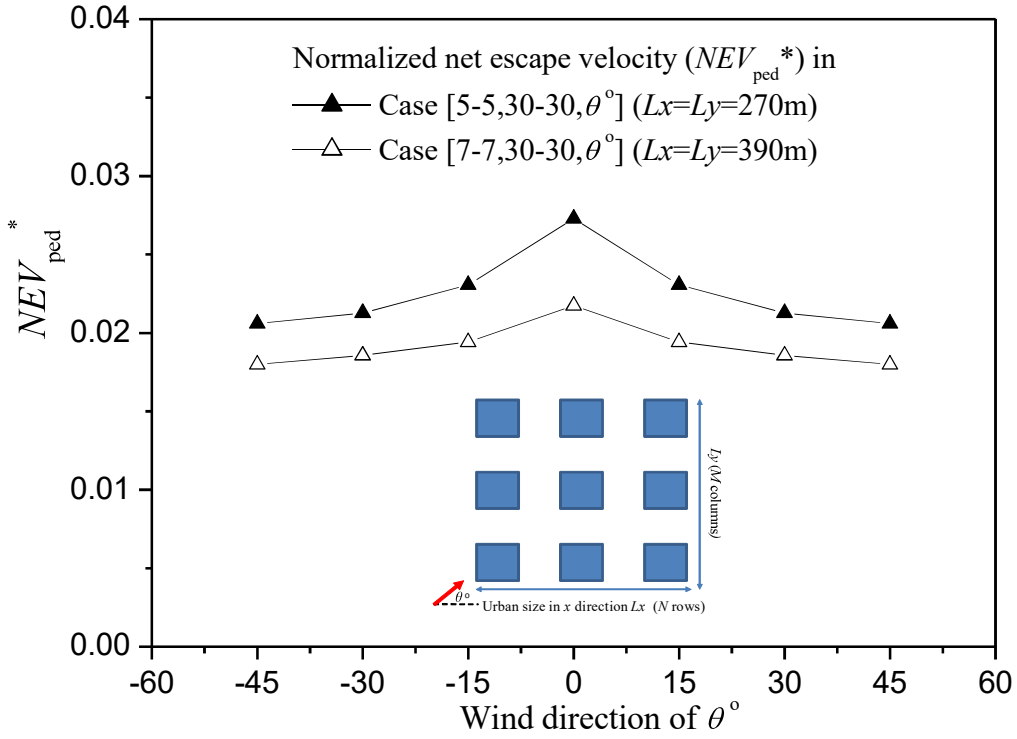

(c)

Fig. 13. In Case [5-5, 30-30, θ] and Case [7-7, 30-30, θ]: (a-b) *PTR* and their *CR*, (c) NEV_{ped}*.

4. Conclusions

This paper investigated the effect of urban size, building height variations, wind direction and wall heating on pollutant removal in 3D idealized urban-like geometries with medium building densities (λ_p=λ_f=0.25). The standard and RNG k-ε models were employed and CFD simulations were validated against wind tunnel data. A new concept, the net escape velocity (*NEV*), was proposed to assess the net capacity of pollutant removal at pedestrian level (about 2m from the ground). Pollutant transport rates (*PTR*) and their ratios (*CR*) were also used to show the relative significance by mean flows and turbulent diffusion across UCL boundaries.

The urban size was found to be the first key factor for *NEV*. In neighbourhood-scale (~1km) models with a parallel approaching wind, after an adjustment region characterized by wind velocity reduction, a fully-developed region occurred where velocity and turbulent quantities remained constant. However, pollutant concentration still slightly increased toward downstream due to a pollutant accumulation effect. Thus, longer UCL models experienced smaller *NEV*. In particular, both turbulent diffusion across street roofs and horizontal mean flows were important for *NEV*, and vertical mean flows contributed less to *NEV* due to pollutant re-entry. On the other

hand, for street-scale (~100m) model, a large part of pollutant was removed by horizontal mean flows, and the flow across lateral UCL boundaries slightly contributed to pollutant removal. In contrast with uniform building height, building height variations reduced the length of the adjustment region, enhanced vertical mean flows, improved pollutant dilution in front of taller buildings but worsened that behind taller buildings and only slightly influenced *NEV*. Finally, the parallel approaching wind and wall heating were found to attain larger *NEV* than oblique wind directions and isothermal conditions.

Although further investigations are still required, this paper explores ways to quantify pollutant removal at pedestrian level in medium-dense urban areas. The combination of *PTR*, *CR* and *NEV* offer a practical tool to map areas of the city where ventilation conditions may be improved by acting on an alteration of the structural form of the city itself or by adding trees or urban vegetation which can be used to modify both the overall form of the street-network and temperature distribution.

Acknowledgements

This study was financially supported by the National Natural Science Foundation of China (No. 51108102) and (No 51478486) as well as special fund of Key Laboratory of Eco Planning & Green Building, Ministry of Education (Tsinghua University), China.

Nomenclature

A_p	total boundary area of a control volume
B,H, L,W	building width, building height, urban size, street width
$\bar{c}$	time-averaged pollutant concentration
F_m , F_t	pollutant fluxes due to mean flow and turbulence (m^{-2})
PTR	normalized pollutant transport rate
FA_m^* , FA_t^*	*PTR* due to mean flow and turbulence
K_c , ν_t	turbulent eddy diffusivity of pollutant and that for momentum
k, ε	turbulence kinetic energy and its dissipation rate
λ_p, λ_f	building packing density, frontal area density

$\dot{M}_0$, $\dot{M}$	total mass release rate (kg/s)
$\vec{n}$	normal direction of street openings or canopy roofs
NEV_{ped}, NEV_{ped}*	pedestrian net escape velocity and its normalized value
PFR_{ped}	pedestrian purging flow rate
σ_H	standard deviations of building height
S_c	pollutant release rate (10^{-7} $kgm^{-3}s^{-1}$)
S_{ct}	turbulent Schmidt number (S_{ct}=0.7)
U_0	velocity in upstream free flow
$\vec{V}$, $\overline{u_j}$, x_j	velocity vector, velocity components, coordinate components
Vol	pedestrian-level air volume
x, y, z	stream-wise, lateral, vertical directions
$\overline{u}$, $\overline{v}$, $\overline{w}$	stream-wise, lateral, vertical velocity components

Reference

[1] Fenger J. Urban air quality. Atmos Environ 1999;33(29):4877-4900.

[2] Luo Z, Li Y, Nazaroff WW. Intake fraction of nonreactive motor vehicle exhaust in Hong Kong. Atmos Environ 2010;44(15):1913-1918.

[3] Ng W, Chau C. A modeling investigation of the impact of street and building configurations on personal air pollutant exposure in isolated deep urban canyons. Sci Total Environ 2014;468-469:429-48.

[4] Chen C, Zhao B, Zhou WT, Jiang XY, Tan ZC. A methodology for predicting particle penetration factor through cracks of windows and doors for actual engineering application. Build Environ 2012;47:339-348.

[5] Bady M, Kato S, Huang H. Towards the application of indoor ventilation efficiency indices to evaluate the air quality of urban areas. Build Environ 2008;43:1991-2004.

[6] Zhang Y, Gu Z. Air quality by urban design. Nat Geosci 2013;6(7):506-506.

[7] Hang J, Li Y, Sandberg M, Buccolieri R, Di Sabatino S. The influence of building height variability on pollutant dispersion and pedestrian ventilation in idealized high-rise urban areas. Build Environ 2012;56:346-360.

[8] Hang J, Sandberg M, Li Y. Age of air and air exchange efficiency in idealized city models. Build Environ 2009;44(8):1714-1723.

[9] Luo Z, Li Y. Passive urban ventilation by combined buoyancy-driven slope flow and wall flow: Parametric CFD studies on idealized city models. Atmos Environ 2011; 45:5946-5956.

[10] Yuan C, Ng E, Norford LK. Improving air quality in high-density cities by understanding the relationship between air pollutant dispersion and urban morphologies. Building Environ 2014;71:245-258.

[11] Yang F, Qian F, Lau S SY. Urban form and density as indicators for summertime outdoor ventilation potential: A case study on high-rise housing in Shanghai. Build Environ 2013;70:122-137.

[12] Hang J, Li Y. Age of air and air exchange efficiency in high-rise urban areas. Atmos Environ 2011;45(31):5572-5585.

[13] Buccolieri R, Sandberg M, Di Sabatino S. City breathability and its link to pollutant concentration distribution within urban-like geometries. Atmos Environ 2010; 44:1894-1903.

[14] Buccolieri R., Salizzoni P., Soulhac L., Garbero V., Di Sabatino S. The breathability of compact cities. Urban Climate 2015;13:73-93.

[15] Britter RE, Hanna SR. Flow and dispersion in urban areas. Annu Rev Fluid Mech 2003; 35: 469-496.

[16] Fernando HJS, Zajic D, Di Sabatino S, Dimitrova R, Hedquist B, Dallman A. Flow, turbulence, and pollutant dispersion in urban atmospheres. Phys Fluids 2010;22(5):051301.

[17] Fan Q , Yu W, Fan SJ, Wang XM, Lan J, Zou DL, Feng YR et al. Process analysis of a regional air pollution episode over Pearl River Delta Region, China, using the MM5-CMAQ model. J Air Waste Manage 2014;64(4):406-418.

[18] Ashie Y, Kono T. Urban-scale CFD analysis in support of a climate-sensitive design for the Tokyo Bay area. Int J Climatol 2011;31(2):174-188.

[19] Oke TR. TR. Street design and urban canopy layer climate. Energy Build 1988;11(1-3):103-113.

[20] Baik JJ, Kim JJ. On the escape of pollutants from urban street canyons. Atmos Environ 2002;36:527-536.

[21] Li XX, Liu CH, Leung DYC. Numerical investigation of pollutant transport characteristics inside deep urban street canyons. Atmos Environ 2009; 43(15): 2410-2418.

[22] Liu CH, Leung DYC, Barth MC. On the prediction of air and pollutant exchange rates in street canyons of different aspect ratio using large-eddy simulation. Atmos Environ 2005; 39:1567-1574.

[23] Liu CH, Wong CCC. On the pollutant removal, dispersion, and entrainment over two-dimensional idealized street canyons. Atmos Res 2014;135-136:128-42.

[24] Grimmond CSB, Oke TR. Aerodynamic properties of urban areas derived, from analysis of surface form. J Appl Meteorol 1999; 38(9): 1262-1292.

[25] Hagishima A, Tanimoto J, Nagayama K, Meno S. Aerodynamic parameters of regular arrays of rectangular blocks with various geometries. Bound-Layer Meteor 2009; 132(2):315-337.

[26] Moonen P, Dorer V, Carmeliet J. Effect of flow unsteadiness on the mean wind flow pattern in an idealized urban environment. J Wind Eng Ind Aerodyn 2012; 104:389-396.

[27] Kim JJ, Baik JJ. A numerical study of the effects of ambient wind direction on flow and dispersion in urban street canyons using the RNG k-ε turbulence model. Atmos Environ 2004;38:3039-3048.

[28] Yassin MF. Numerical modeling on air quality in an urban environment with changes of the aspect ratio and wind direction. Environ Sci Pollut R 2013;20(6):3975-3988.

[29] Hang J, Luo Z, Sandberg M, Gong J. Natural ventilation assessment in typical open and semi-open urban environments under various wind directions. Build Environ 2013; 70: 318-333.

[30] Di Sabatino S., Buccolieri R., Salizzoni P. Recent advancements in numerical modelling of flow and dispersion in urban areas: a short review. Int. J. Environment and Pollution 2013;52:172-191.

[31] Yang L, Li Y. City ventilation of Hong Kong at no-wind conditions. Atmos Environ 2009;43:3111-3121.

[32] Liu J, Luo Z, Zhao J, Shui T. Ventilation in a street canyon under diurnal heating conditions. Int J Vent 2012;11(2):141-154.

[33] Xie X, Liu CH and Leung DYC. Impact of building facades and ground heating on wind flow and pollutant transport in street canyons. Atmos Environ 2007;41:9030-9049.

[34] Cai X. Effects of differential wall heating in street canyons on dispersion and ventilation characteristics of a passive scalar. Atmos Environ 2012;51:268-277.

[35] Yang X, Li Y, Yang L. Predicting and understanding temporal 3D exterior surface temperature distribution in an ideal courtyard. Build Environ 2012;57:38-48.

[36] Allegrini J, Dorer V, Carmeliet J. Buoyant flows in street canyons: Validation of CFD simulations with wind tunnel measurements. Build Environ 2014;72:63-74.

[37] Allegrini J, Dorer V, Carmeliet J. Wind tunnel measurements of buoyant flows in street canyons. Build Environ 2013;59:315-26.

[38] Li XX, Britter RE, Norford LK, Koh TY, Entekhabi D. Flow and pollutant transport in urban street canyons of different aspect ratios with ground heating: large-Eddy simulation. Bound-Layer Meteor 2012,;142(2):289–304.

[39] Memon RA, Leung DYC, Liu CH. Effects of building aspect ratio and wind speed on air temperatures in urban-like street canyons. Build Environ 2010;45(1):176-188.

[40] Stavrakakis GM, Zervas PL, Sarimveis H, Markatos NC. Development of a computational tool to quantify architectural-design effects on thermal comfort in naturally ventilated rural houses. Build Environ 2010;45(1):65–80.

[41] Lim ES, Ito K, Sandberg M. New ventilation index for evaluating imperfect mixing conditions - Analysis of Net Escape Velocity based on RANS approach. Build Environ 2013;61:45-56.

[42] FLUENT V6.3. User's Manual.2006. http://www.fluent.com.

[43] Yoshie R, Mochida A, Tominaga Y, Kataoka H, Harimoto K, Nozu T, Shirasawa T. Cooperative project for CFD prediction of pedestrian wind environment in the Architectural Institute of Japan. J Wind Eng Ind Aerodyn 2007;95:1551-1578.

[44] Lien FS, Yee E. Numerical modeling of the turbulent flow developing within and over a 3-D building array, part I: A high-resolution Reynolds-averaged Navier-Stokes approach. Boundary-layer Meteorol 112;2004:427-466.

[45] Hang J, Li Y. Wind conditions in idealized building clusters – macroscopic simulations using a porous turbulence model. Boundary-Layer Meteorol 2010;136(1):129-159.

[46] Giovannini L, Zardi D, De Franceschi M.D. Characterization of the thermal structure inside an urban canyon: Field measurements and validation of a simple model. J. Appl. Meteor. Climatol. 2013;52:64-81.

[47] Argyropoulos, CD, Markatos, N.C. Recent advances on the numerical modelling of turbulent flows. App Math Model 2015;39(2):693–732.

[48] Blocken, B. 50 years of Computational Wind Engineering: Past, present and future. J Wind Eng Ind Aerodyn 2014;129:69-102.

[49] Blocken B, Stathopoulos T, Carmeliet J. CFD simulation of the atmospheric boundary layer: wall function problems. Atmos Environ 2007; 41:238-252.

[50] van Hooff T, Blocken B. CFD evaluation of natural ventilation of indoor environments by the concentration decay method: CO2 gas dispersion from a semi-enclosed stadium. Build Environ 2013; 61:1-17.

[51] van Hooff T, Blocken B. On the effect of wind direction and urban surroundings on natural ventilation of a large semi-enclosed stadium. Computers & Fluids 2010; 39:1146-1155.

[52] Tominaga Y, Mochida A, Yoshie R, Kataoka H, Nozu T, Yoshikawa M, et al. AIJ guidelines for practical applications of CFD to pedestrian wind environment around buildings. J Wind Eng Ind Aerodyn 2008;96:1749-1761.

[53] Grimmond CSB, Oke TR. Turbulent heat fluxes in urban areas: observations and a Local-Scale Urban Meteorological Parameterization Scheme (LUMPS). J Appl Meteorol 2002;41:792-810.

[54] Gao NP, Niu JL. CFD study of the thermal environment around a human body: a review. Indoor Built Environ 2005;14:5-16.

[55] Santiago JL, Krayenhoff ES, Martilli A., Flow simulations for simplified urban configurations with microscale distributions of surface thermal forcing, Urban Climate 2014;9:115-133.

[56] Sandberg M, Sjöberg M. The use of moment for assessing air quality in ventilated rooms. Build Environ 1983;18:181-197.

[57] Etheridge D, Sandberg M. Building Ventilation: Theory and Measurement. John Wiley & Sons, Chichester. 1996, p.573-633.

[58]Kato S, Ito K, Murakami S. Analysis of visitation frequency through article tracking method based on LES and model experiment. Indoor Air 2003;13:182-193.

[59]Chen Q. Ventilation performance prediction for buildings: a method overview and recent applications. Build Environ 2009; 44:848-858.

[60] Belcher S, Jerram N, Hunt J, Adjustment of turbulent boundary layer to a canopy of roughness elements, J Fluid Mech 2003;488:369-368.

Figure BW

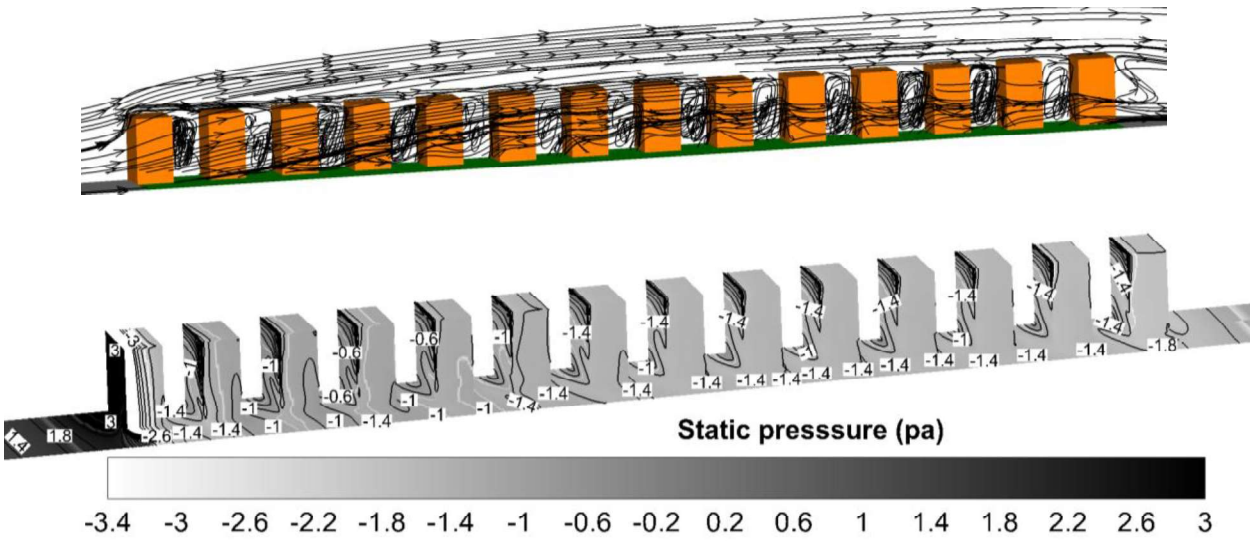
Static presssure (pa)
-3.4 -3 -2.6 -2.2 -1.8 -1.4 -1 -0.6 -0.2 0.2 0.6 1 1.4 1.8 2.2 2.6 3

(a)

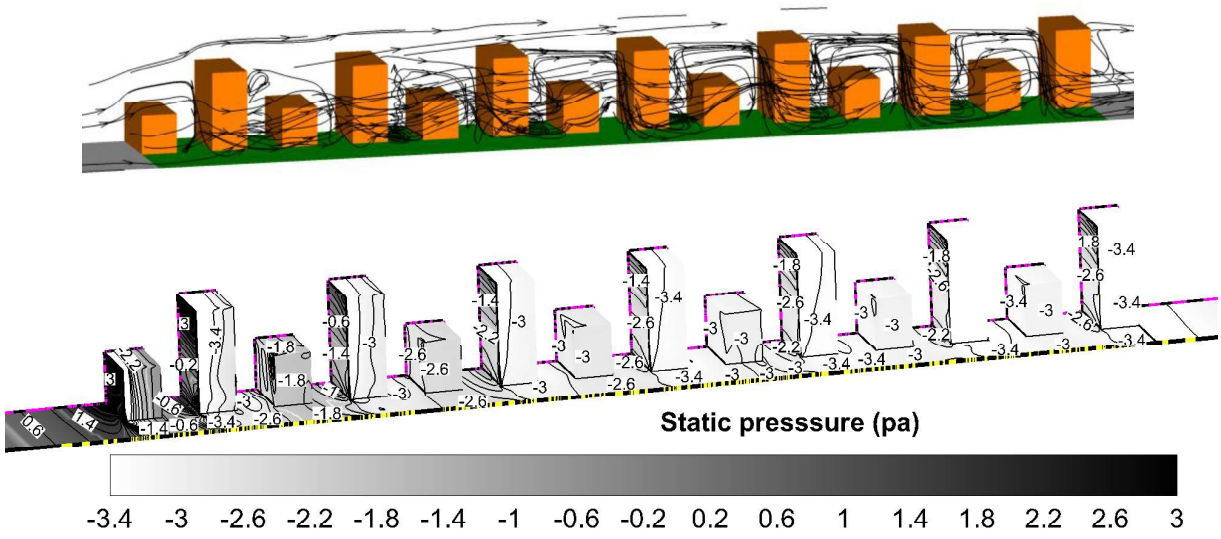
Static presssure (pa)
-3.4 -3 -2.6 -2.2 -1.8 -1.4 -1 -0.6 -0.2 0.2 0.6 1 1.4 1.8 2.2 2.6 3

(b)

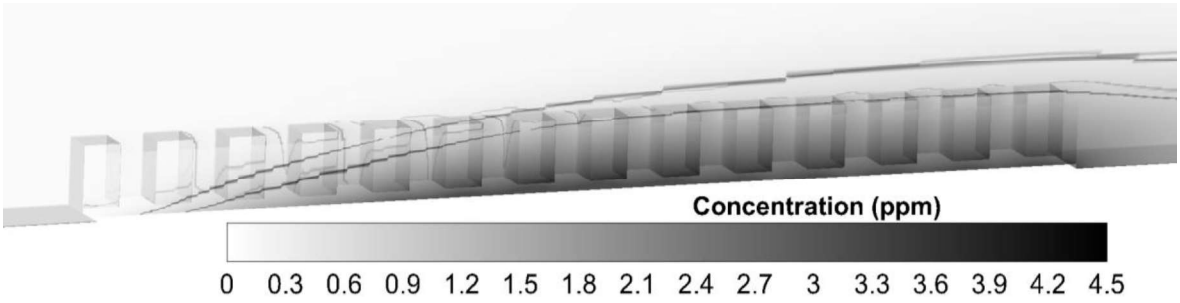
Concentration (ppm)
0 0.3 0.6 0.9 1.2 1.5 1.8 2.1 2.4 2.7 3 3.3 3.6 3.9 4.2 4.5

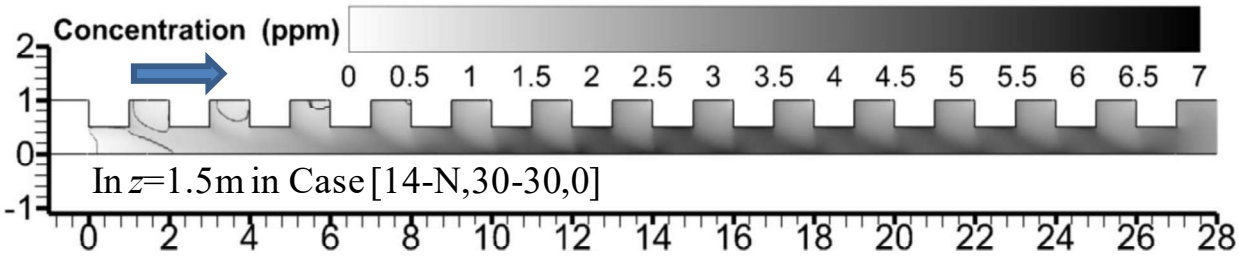

(c)

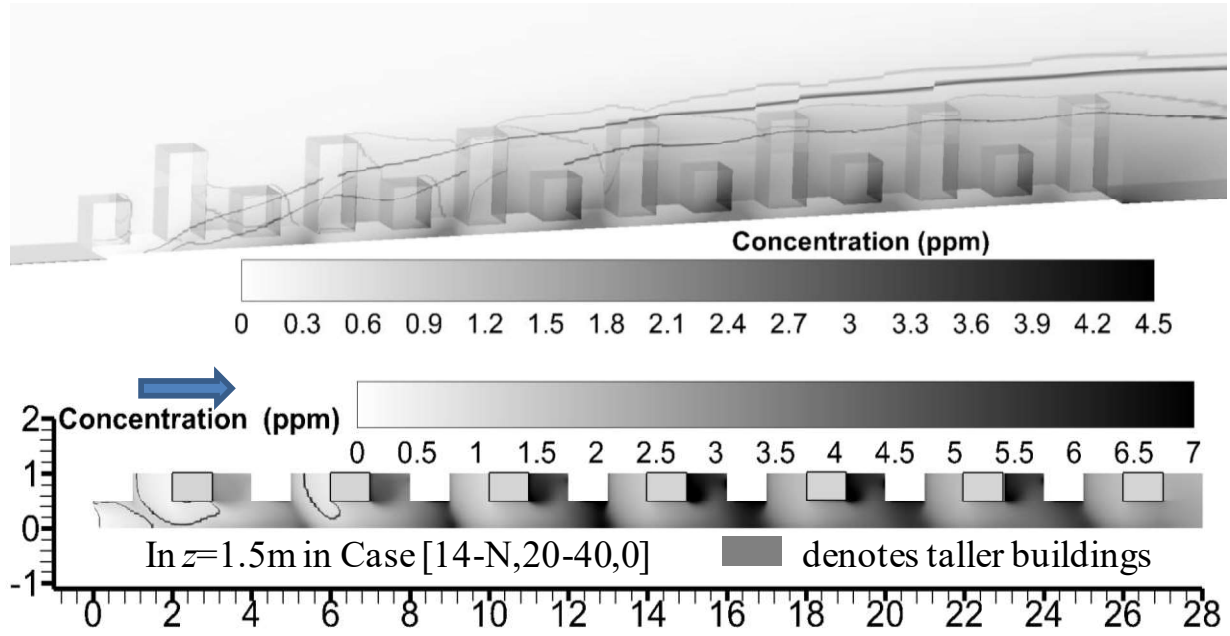

(d)

Fig. 5. Hang et al.

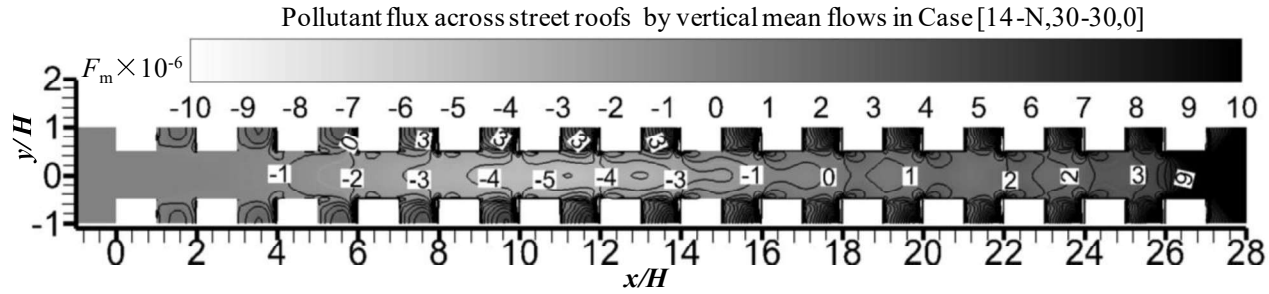

(a)

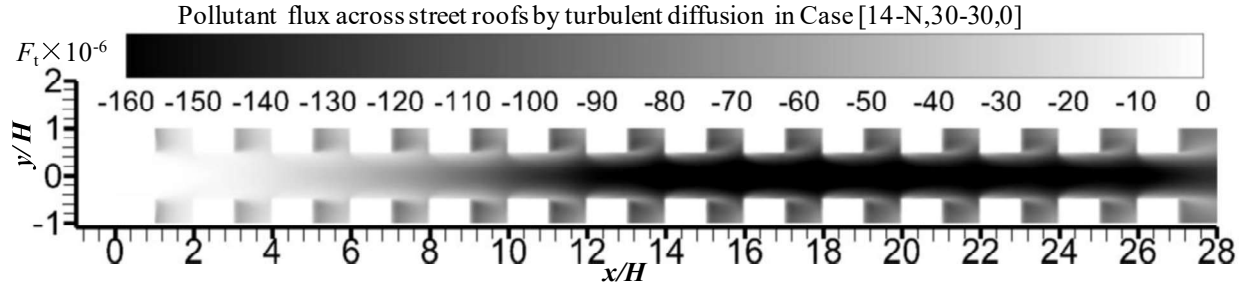

(b)

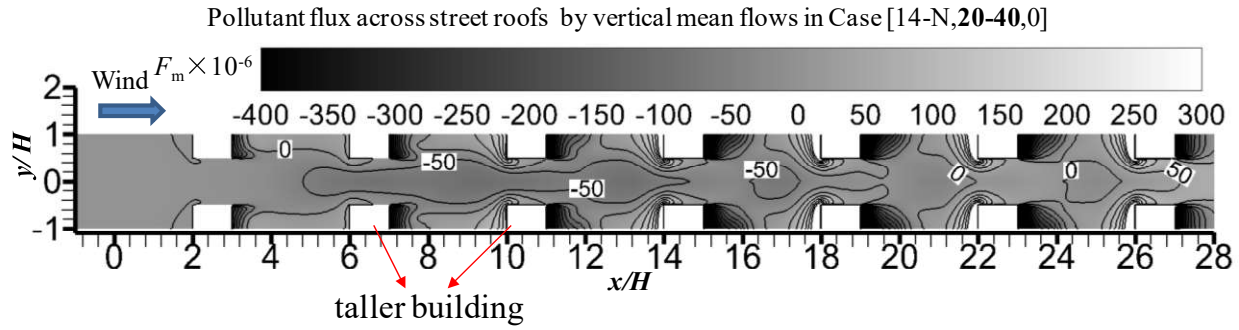

(c)

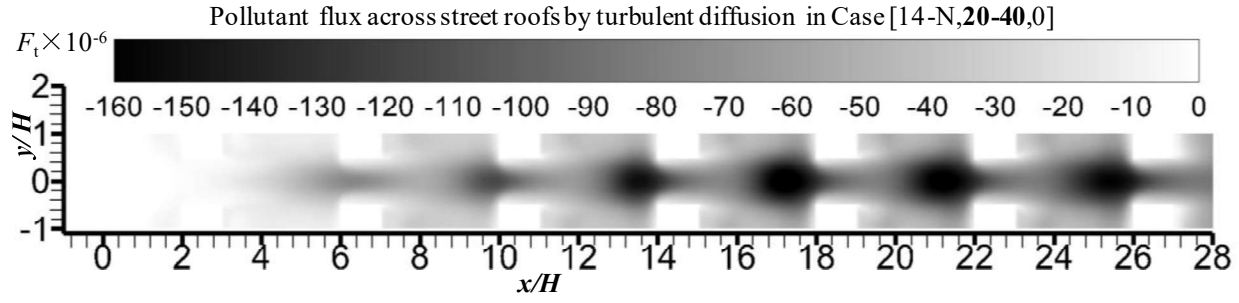

(d)

Fig. 6. Hang et al.

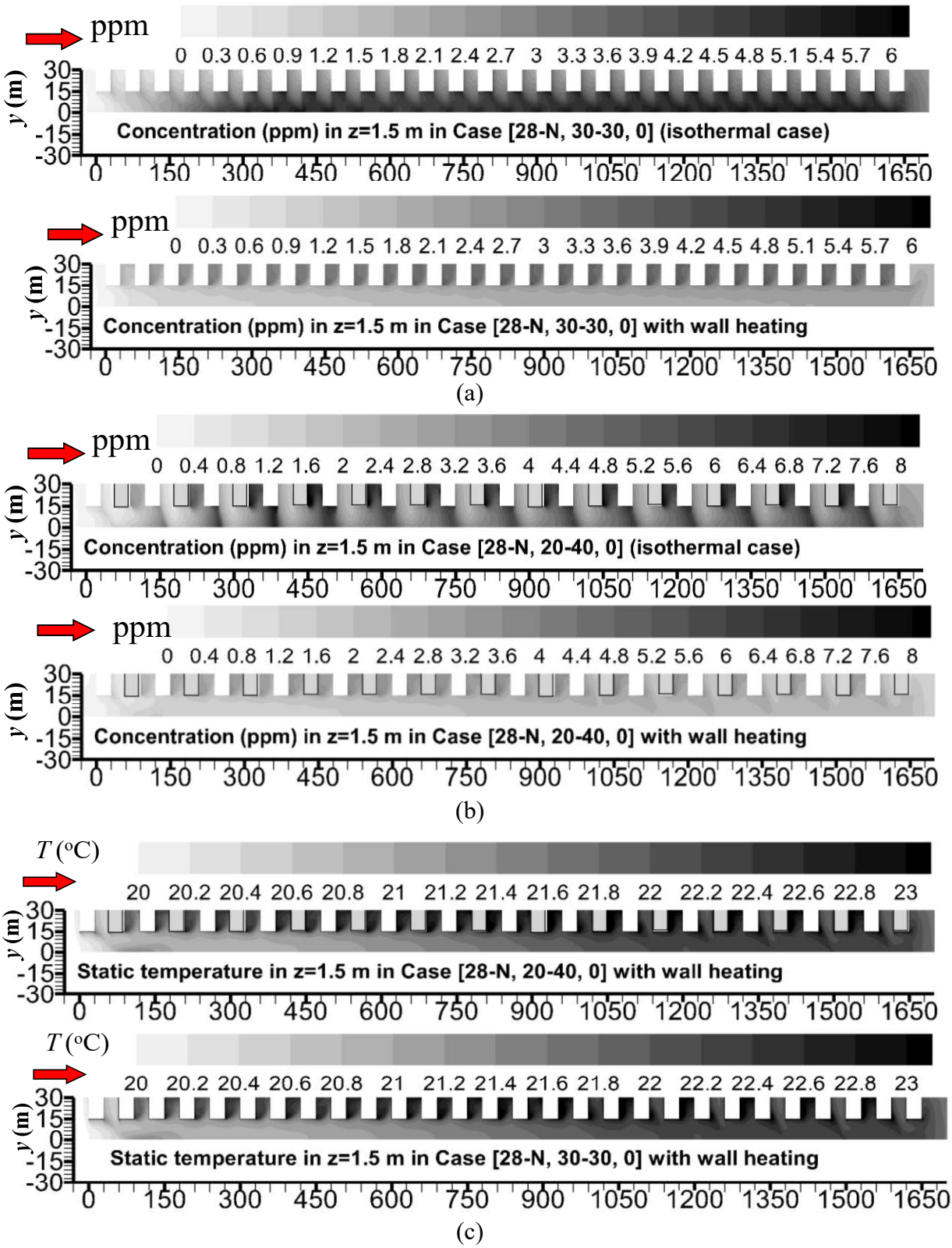

Fig. 8. Hang et al.

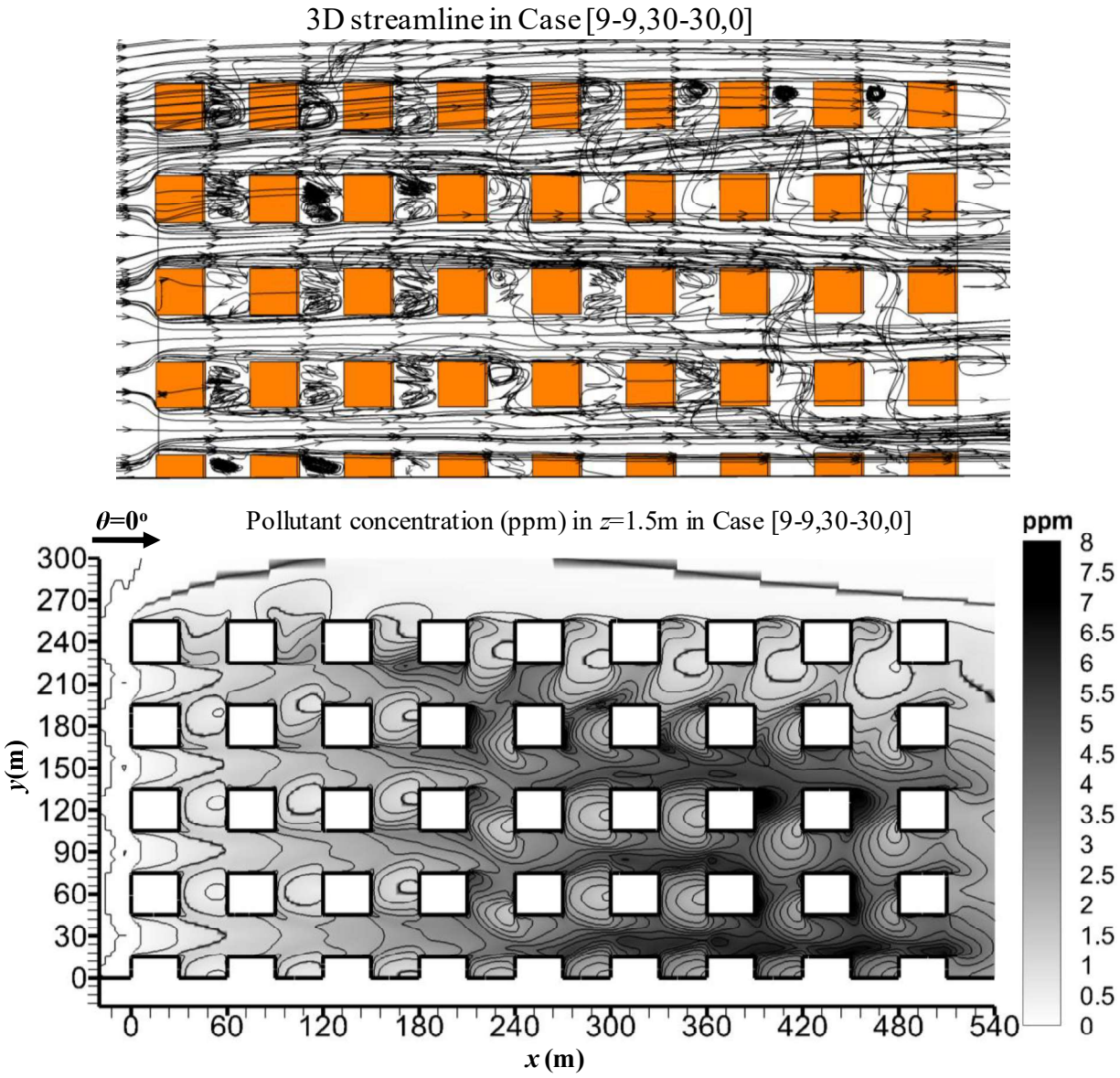

(a)

Fig.11. Hang et al.

In plane of z=1.5m in Case [5-5,30-30,0]

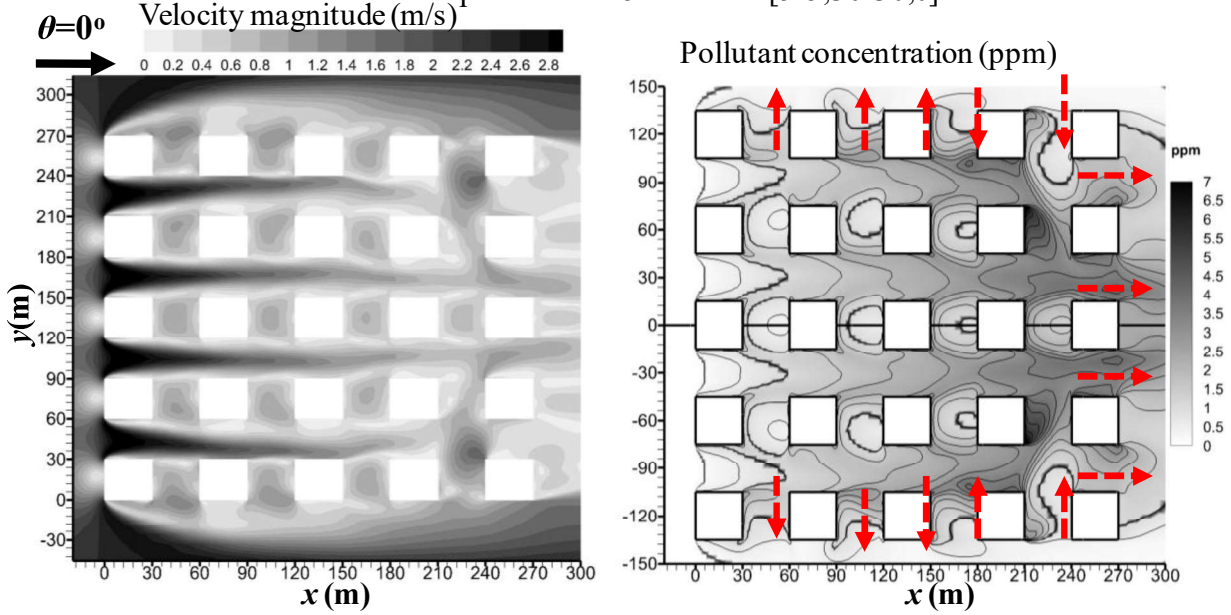

(a)

In plane of z=1.5m in Case [5-5,30-30,15]

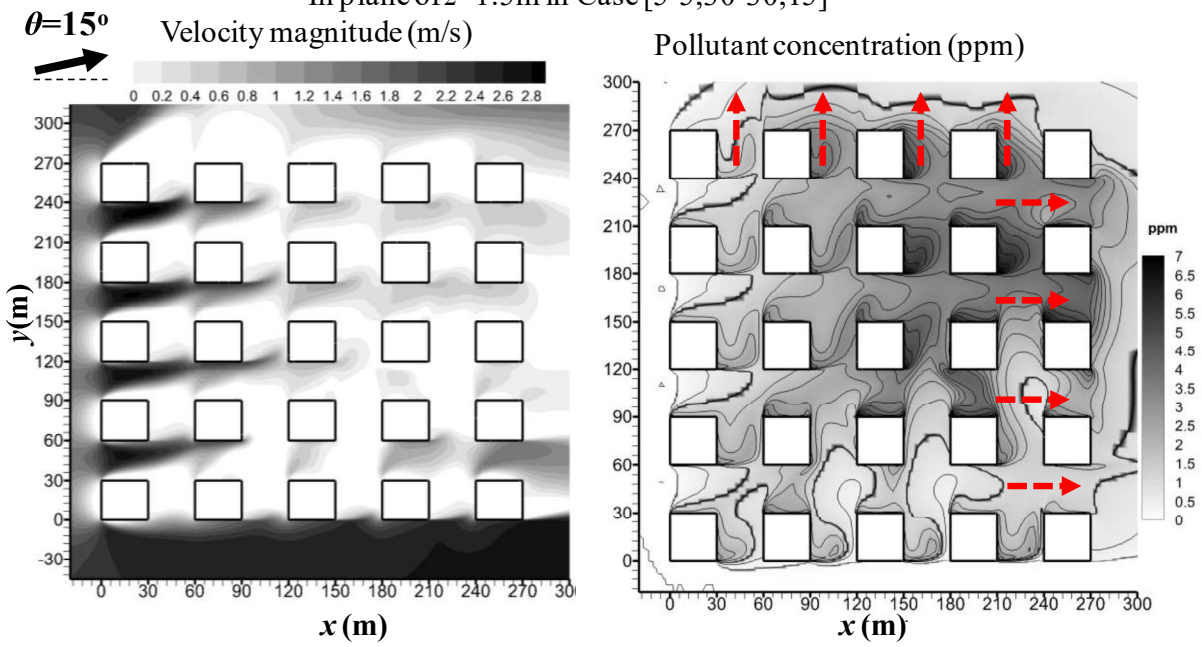

(b)

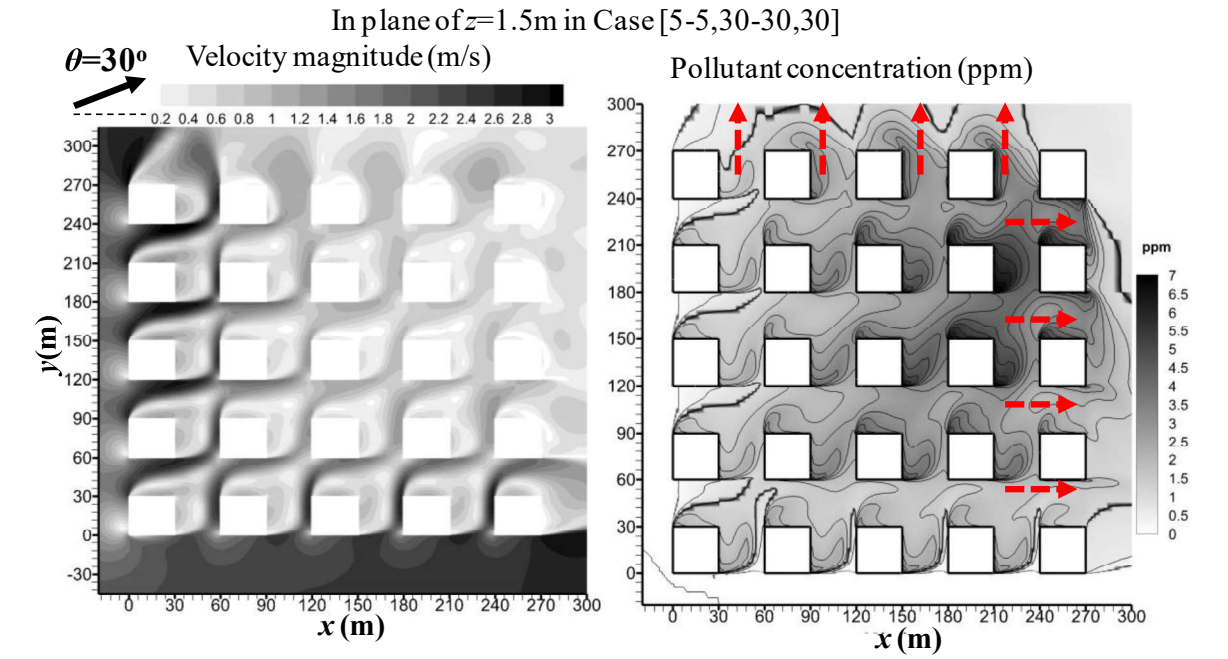

(c)

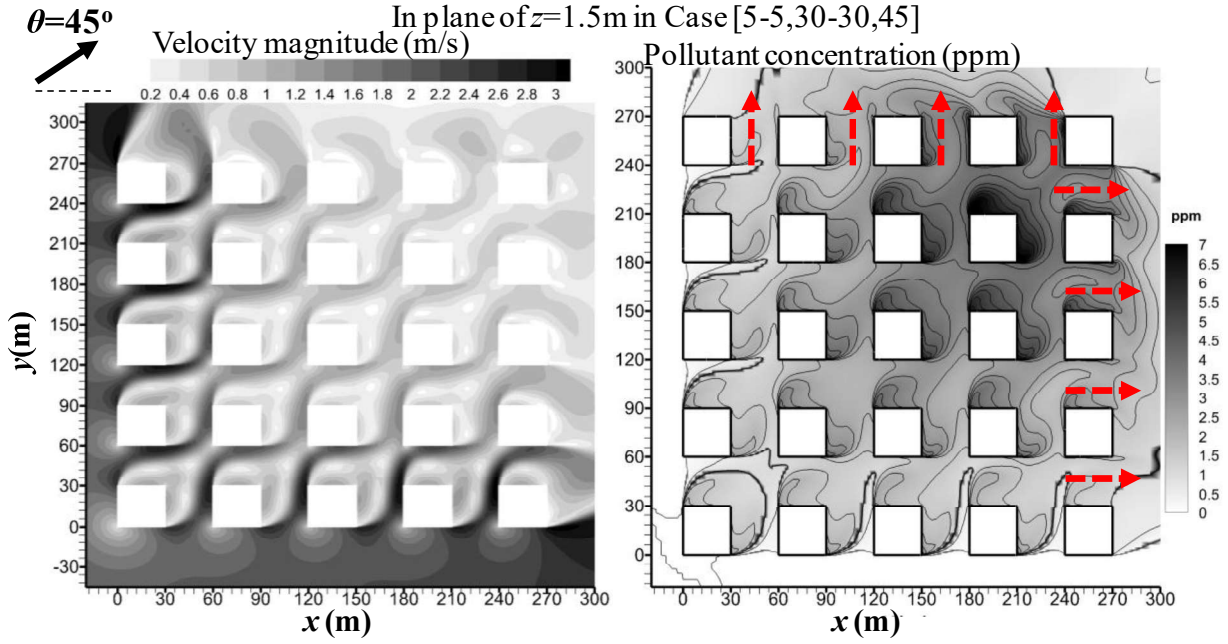

(d)

Fig. 12. Hang et al.